

# Effect of Presodiation Additive on Structural and Interfacial Stability of Hard Carbon | P2-Na<sub>0.66</sub>Mn<sub>0.75</sub>Ni<sub>0.2</sub>Mg<sub>0.05</sub>O<sub>2</sub> Full Cell

Leonardo Sbrascini,<sup>[a, b]</sup> Angelina Sarapulova,<sup>[b]</sup> Cornelius Gauckler,<sup>[c]</sup> Lydia Gehrlein,<sup>[b]</sup> Fabian Jeschull,<sup>[b]</sup> Tolga Akçay,<sup>[b]</sup> Reiner Mönig,<sup>[b]</sup> Mario Marinaro,<sup>\*[c]</sup> Francesco Nobili,<sup>\*[a, d]</sup> and Sonia Dsoke<sup>\*[b, e, f]</sup>

The compatibility between a corncob-derived hard carbon anode and a layered oxide cathode (Na<sub>0.66</sub>Mn<sub>0.75</sub>Ni<sub>0.2</sub>Mg<sub>0.05</sub>O<sub>2</sub>), as well as the effect of presodiation via cathode additive (Na<sub>2</sub>C<sub>4</sub>O<sub>4</sub>), are investigated in a sodium-ion full cell. Extensive physico-chemical and electrochemical characterizations are performed to deeply investigate the structural and interfacial evolution of the materials in the presodiated cell, either within the single cycle or upon long-term cycling. The use of sacrificial cathode additives is generally regarded as a method to improve full cell performance, especially when using sodium-deficient materials. However, undesired effects upon decomposition of the sacrificial salt may arise due to the complexity of the system. In this

study, it is evidenced that the presodiation changes the properties of the electrodes causing a worsening of the electrochemical performance of the cell during long-term cycling. The surface morphology of the cathode is negatively affected by the formation of holes/cracks, while redox processes associated with structural transformations are suppressed in the voltage window of interest, with partial structural deformations occurring during activation cycles. The SEI and CEI are also affected by the formation of insulating organic species, which lead to an increased thickness and interphase resistance hampering the charge transfer kinetics of the cell.

## Introduction

Because of the increasing depletion of fossil fuels and the advancement of global warming, renewable energy sources

such as wind and solar energy are being developed as alternative technologies for electrical energy production.<sup>[1]</sup> However, the intermittent nature of these sources causes an alternating supply of electricity to the grid, which is not compatible with electrical energy usage in homes, transportation, industries, and offices.<sup>[2–4]</sup> Therefore, large-scale energy storage systems (ESSs) are crucial for the proper utilization of renewables.<sup>[5–7]</sup> Among all the storage technologies, rechargeable batteries are attracting the most attention due to their high round-trip efficiency and long cycle life.<sup>[8,9]</sup> For stationary energy storage applications, the ability to store energies of the order of MWh or sometimes even GWh is necessary, which requires the production of extremely large batteries. Consequently, material abundance, cost, and safety are the primary concerns for large-scale electricity storage, rather than energy density.<sup>[10,11]</sup> In contrast to lithium, sodium is widely distributed and abundant in the Earth's crust, and it is considered the most appropriate to fabricate devices for stationary storage.<sup>[12–14]</sup> Sodium-ion batteries offer advantages in terms of costs and resources over their lithium counterparts, and innovations in this field have been strongly encouraged,<sup>[15]</sup> with much effort devoted to the development of suitable electrode materials.

Layered transition metal oxides are some of the most successful cathode materials for commercial LIBs. This class of compounds is also of particular interest for SIBs due to their high specific capacity, the number of possible redox-active metals, and the possibility to use established synthetic procedures.<sup>[16–19]</sup> Currently, different cathode materials are being considered in order to achieve SIBs with high performance. Besides layered transition metal oxides, Prussian blue analogues

[a] L. Sbrascini, F. Nobili

School of Science and Technologies - Chemistry Division, University of Camerino, Via Madonna Delle Carceri - ChIP, Camerino 62032, Italy  
E-mail: francesco.nobili@unicam.it

[b] L. Sbrascini, A. Sarapulova, L. Gehrlein, F. Jeschull, T. Akçay, R. Mönig, S. Dsoke

Institute for Applied Materials (IAM), Karlsruhe Institute of Technology (KIT), Hermann-Von-Helmholtz-Platz 1, D-76344 Eggenstein-Leopoldshafen, Germany

[c] C. Gauckler, M. Marinaro

Zentrum Für Sonnenenergie Und Wasserstoff Forschung Baden-Württemberg (ZSW), Helmholtzstraße 8, 89081 Ulm, Germany  
E-mail: mario.marinaro@zsw-bw.de

[d] F. Nobili

GISEL - Centro di Riferimento Nazionale per i Sistemi di Accumulo Elettrolitico di Energia/NSTM, Firenze 50121, Italy

[e] S. Dsoke

Albert-Ludwigs-University Freiburg, Department of Sustainable Systems Engineering (INATECH), Emmy-Noether-Straße 2, 79110 Freiburg, Germany  
E-mail: sonia.dsoke@inatech.uni-freiburg.de

[f] S. Dsoke

Fraunhofer Institute for Solar Energy Systems, Department Electrical Energy Storage, Heidenhofstr 2, 79110 Freiburg, Germany

Supporting information for this article is available on the WWW under <https://doi.org/10.1002/batt.202400207>

© 2024 The Authors. Batteries & Supercaps published by Wiley-VCH GmbH. This is an open access article under the terms of the Creative Commons Attribution License, which permits use, distribution and reproduction in any medium, provided the original work is properly cited.

and polyanionic compounds<sup>[20–22]</sup> are under consideration. The abovementioned material classes exhibit critical aspects that need careful consideration, including intrinsic water, potential toxicity, low specific capacity, or poor capacity retention. On the other hand, layered oxides suffer from irreversible phase transitions and high reactivity towards moisture, making an evaluation of the chemical composition essential to obtain optimal cathode materials for this class of compounds.

Regarding the choice of transition metal (TM) cations for the cathode composition, Mn and Fe have the highest abundance and the lowest price, with Mn showing the lowest price turbulence thanks to its wide distribution. Mn ions can contribute to capacity as a redox center or work as a structural scaffold when kept in the 4+ oxidation state. When considering the number of transferred electrons by the redox-active species and the average working potential, the Ni<sup>4+</sup>/Ni<sup>2+</sup> redox couple possesses the highest average potential and can achieve a high specific energy density, making it one of the most favorable active elements to be employed.<sup>[23]</sup> Depending on the surrounding Na environment and the number of unique oxide packings, Na layered oxides can generally be classified as O3- or P2-phase, with the letter indicating the site where Na<sup>+</sup> ions are located (i.e., O=octahedral; P=prismatic) and the number indicating how many unique interlayers are surrounded by the different oxide layers.<sup>[24]</sup> The P2-phase generally displays better overall electrochemistry than the O3-phase, thanks to its low diffusion barrier and high ionic conductivity.<sup>[25–28]</sup> However, P2-type layered oxides are prone to phase transformations upon cycling. These can be attributed to several factors: (I) electronic structural changes of cations and oxygen, leading to anisotropic distortions<sup>[29]</sup> (e.g., Jahn-Teller-active Mn<sup>3+</sup>); (II) cation migration,<sup>[30,31]</sup> (III) unbalancing of electrostatic interactions between the O–O repulsion, O–Na attraction, and van der Waals force, which lead to P-type to O-type phase transitions<sup>[32,33]</sup> (e.g. Ni<sup>4+</sup>/Ni<sup>2+</sup> redox couple). While these phase transitions are unlikely to be entirely suppressed, they can be significantly mitigated or stabilized by cation substitution.<sup>[34–37]</sup> Moreover, the sodium deficiency due to lower Na stoichiometry (0.7 > x > 0.6 in Na<sub>x</sub>MO<sub>2</sub>) makes their application in full cells quite difficult, as the practical capacity of the cathode is limited.

Hard carbons are considered as the best choice for the anode side due to the possibility of producing them from waste biomass.<sup>[38–40]</sup> However, a significant first cycle irreversible capacity is typically observed due to SEI formation and Na-ion trapping in the material,<sup>[41]</sup> resulting in the loss of cyclable sodium when in a full cell configuration. Up to now, the highest reported coulombic efficiencies for commercial hard carbons at the first cycle are around 85%,<sup>[42,43]</sup> meaning that at least 15% cyclable sodium is irreversibly lost even in the best-case scenario. The addition of cathode excess to (I) balance the irreversible capacity from SEI formation and (II) address the sodium deficiency to balance the anode reversible capacity, would increase the costs for cell manufacture and leave part of the cathode as dead weight after the first cycle, reducing the cell energy density. Therefore, presodiation strategies have been studied for full cell applications, which mainly involve direct contact with Na metal or electrochemical precycling in

half-cell.<sup>[44,45]</sup> However, these methods are suitable for lab-scale applications but difficult to employ on a larger scale.

Recently, the use of sacrificial sodium sources as additives in the positive electrode formulation has gained increasing attention, with several compounds studied for this purpose,<sup>[46–54]</sup> since they allow to obtain a voltage-induced in-situ premetallation. Among these, the use of Na-squarate is considered as a cheap, green, and easy-to-prepare solution for presodiation, as it undergoes irreversible oxidative decomposition with release of Na<sup>+</sup> at 3.6 V vs Na<sup>+</sup>/Na.<sup>[52,55,56]</sup> Still, although beneficial effects are generally evidenced, sodium squarate has been mostly reported for use in capacitors,<sup>[55,56]</sup> while it has been seldom used in sodium-ion batteries, where cathodes without sodium deficiency are more frequently employed (e.g., NVP or NVPF),<sup>[52,57,58]</sup> disregarding possible negative effects arising from different choices of electrode materials. Moreover, when considering layered oxide cathodes, factors like electrode mass loadings, number of cycles and upper cut-off voltage (with associated phase transitions) are often not considered, making the transposition of results from half-cells to full cells useful, but still far from real applications.<sup>[59]</sup>

This work presents the application of a layered P2-type Na<sub>0.66</sub>Mn<sub>0.75</sub>Ni<sub>0.2</sub>Mg<sub>0.05</sub>O<sub>2</sub> cathode (NaMNMO)<sup>[60]</sup> and a corn-cob-derived hard carbon (CCDHC) [61] for use in a sodium-ion full cell, along with a compatibility study with a presodiation method that employs sodium squarate sacrificial salt (Na<sub>2</sub>C<sub>4</sub>O<sub>4</sub>). Focusing on the use of high-loading electrodes (about 10 mg cm<sup>-2</sup> for the cathode and about 7 mg cm<sup>-2</sup> for the anode), this study includes an extensive analysis of the structural, interfacial, and electrochemical characteristics of the electrodes when used in a full cell configuration with Na<sub>2</sub>C<sub>4</sub>O<sub>4</sub> as the presodiation source. The systems with and without presodiation are tested for a relatively high number of cycles as compared to similar literature,<sup>[59]</sup> and within a voltage region that is generally quite critical for material fatigue and electrolyte degradation,<sup>[62]</sup> trying to identify the structure-property relationships under these conditions through in-depth characterizations.

## Results and Discussion

### Structural Analysis of NaMNMO and Na<sub>2</sub>C<sub>4</sub>O<sub>4</sub>

The structure of NaMNMO was investigated by X-Ray diffraction (XRD) analysis. As a result of the Rietveld refinement, the crystallographic parameters are reported in Figure S1.

The diffraction pattern from Figure S1a can be addressed to a P2-type structure with hexagonal lattice and space group *P6<sub>3</sub>/mm*. All reflections on the diffractogram have been indexed by using a model of the prototype structure ICDD PDF 01–070–3726. The 10 *l* reflections (i.e., 102, 104, 106, 108) display asymmetric peak broadening, indicating the presence of stacking faults in the structure. In fact, the ideal P2 structure should possess transition metals arranged in a CC fashion with oxygen in an AB BA sequence. As proposed in the literature, the material displays a stacking fault with a (2/3 1/3 1/2) transition vector, which changes the stacking sequence of the metals

from CC to CA, resulting in the observed peak broadening of 10 *l* reflections (Figure S1b). These layered structure defects are described in the previous works on the same material.<sup>[60,63]</sup>

The Rietveld analysis from the diffraction data of the as-synthesized Na<sub>2</sub>C<sub>4</sub>O<sub>4</sub> structure (Figure S2) confirms that it is crystallized with a primitive monoclinic unit cell belonging to the *P2<sub>1</sub>/c* space group without any impurities.<sup>[64]</sup>

### Electrochemical Characterization

The electrochemical characterization of the materials in half-cells and full cells was performed either with or without the use of sodium squarate as the additive for presodiation; the mass loadings of all electrodes tested in this work ranged from 9–11 mg cm<sup>-2</sup> for the cathodes and 6–7 mg cm<sup>-2</sup> for the anodes. To make the discussion clearer, the labels for each cell type used from now on are reported in Table 1.

Electrodes of NaMnMO and CCDHC were subjected to cyclic voltammetry (CV) and rate capability test in half-cells vs. Na, to investigate the redox processes occurring during Na storage and assess the specific capacities of the single cathode and anode materials. However, several studies in the literature suggest the use of electrolyte additives like fluoroethylene carbonate (FEC), pointing out the instability of sodium metal when used as the counter electrode in half-cells.<sup>[65,66]</sup> Hence, the effect of FEC additive was firstly investigated at different specific currents, monitoring the Na plating/stripping at the counter electrode. Since the obtained results confirmed the low stability of the Na metal counter electrode upon cycling without FEC additive (refer to Figure S3 in the *Supporting Information* for further details), all half-cell measurements were performed by employing 5% FEC additive in the electrolyte.

The redox processes occurring during Na storage into electrodes of NaMnMO and CCDHC were investigated via cyclic voltammetry (CV) at a scan rate of 0.1 mV s<sup>-1</sup> in half-cells vs. Na within the potential window of 2.70–4.30 V and 0.01–1.5 V, respectively. The results obtained for both measurements are shown in Figure S4. The anodic and cathodic scans from the voltammograms in Figure S4a display the characteristic features of sodium storage in NaMnMO. The Mn<sup>3+</sup>/Mn<sup>4+</sup> redox couple was purposely cut out from the working potential window of the material, allowing Mn to stay in +4 oxidation state and avoiding the presence of Jahn-Teller-active Mn<sup>3+</sup> ions or dismutation into soluble Mn<sup>2+</sup> ions,<sup>[67]</sup> thus sacrificing a small amount of capacity to provide a higher structural stability upon

cycling. Briefly, during the first anodic scan, two peaks in the 3.20–3.90 V potential region can be indexed to Ni redox activity, with oxidation of Ni<sup>2+</sup> to Ni<sup>3+</sup> and then to Ni<sup>4+</sup>.<sup>[68,69]</sup> The additional intense peak centered at 4.20 V is related to the phase transition from P2 towards an O2-type structure.<sup>[70]</sup> As shown in a previous study, the presence of electrochemically inactive Mg as a dopant in the structure prevents the complete P2-O2 phase transition, favoring and stabilizing the formation of multiple intermediate phases between the two structures generally called Z-phase.<sup>[60]</sup> During the first cathodic scan, the presence of a peak in the high voltage region (*E* = 4.00 V) is attributed to the transition from the Z-phase back to the P2 phase,<sup>[71]</sup> confirming the reversibility of the transition. Finally, the two peaks at *E* = 3.60 V and *E* = 3.30 V are associated with the reduction of Ni<sup>4+</sup> to Ni<sup>3+</sup> and then to Ni<sup>2+</sup>, respectively.<sup>[68,69]</sup> All processes from the second cycle onwards are repeated and superimposed, indicating a high reversibility of the redox processes upon cycling.

The voltammograms in Figure S4b display the characteristic features of sodium storage into hard carbons. Briefly, the broad peak upon sodiation, centered at 0.35 V and starting at approximately 0.7 V, is attributed to the formation of the SEI layer due to electrolyte decomposition at the anode surface. The disappearance of this process in subsequent cycles indicates that the SEI is fully formed after the first cycle. The two other peaks represent the typical Na<sup>+</sup> adsorption-intercalation processes in hard carbons. Since the sodiation/desodiation mechanism in hard carbons is still poorly understood, and several models can be found in the literature,<sup>[72]</sup> the accurate attribution of these signals to the correct process is generally not easy. However, in a recently published work,<sup>[61]</sup> an extensive characterization of the charge storage mechanism in CCDHC when used as anode material for Na-ion batteries was carried out, evidencing that the high-potential region (0.15 V < *E* < 0.75 V) is mainly controlled by surface adsorption phenomena, while for the low potential region (*E* < 0.15 V) diffusion processes are the dominant ones, hence being consistent with Na-ion intercalation into the carbon framework. Upon desodiation, the peak centered at 0.25 V and the enlarged peak at *E* > 0.25 V represent Na<sup>+</sup> ion deintercalation and desorption from the carbon matrix, respectively. After the first cycle, all the processes except the SEI formation are repeated and superimposed, suggesting high reversibility.

In order to assess the tolerance of NaMnMO and CCDHC to both low and high currents, the rate capabilities of the materials were also evaluated. In detail, specific currents of 10, 20, 40, 100, 400, 1000 and 2000 mA g<sup>-1</sup> have been applied, with current rate changing every 5<sup>th</sup> cycle; subsequently, a specific current of 20 mA g<sup>-1</sup> has been restored in order to verify the capacity retention of the material. The results of the rate capability tests are shown in Figure 1.

Up to a current rate of 100 mA g<sup>-1</sup>, the specific capacity of NaMnMO experiences only a minor decline, while at higher rates the decrease becomes more significant (Figure 1a). After the 6<sup>th</sup> cycle, as the specific current is progressively increased up to 5 times (i.e., from 20 to 100 mA g<sup>-1</sup>), the capacity retention of the layered oxide remains as high as 88%. The

**Table 1.** Adopted labels for all cells reported.

Cell type	Label
Cathode half-cell	NaMnMO
Cathode + Na <sub>2</sub> C <sub>4</sub> O <sub>4</sub> half-cell	NaMnMO-SSq
Anode half-cell	CCDHC
Full cell	CCDHC    NaMnMO
Full cell with Na <sub>2</sub> C <sub>4</sub> O <sub>4</sub>	CCDHC    NaMnMO-SSq

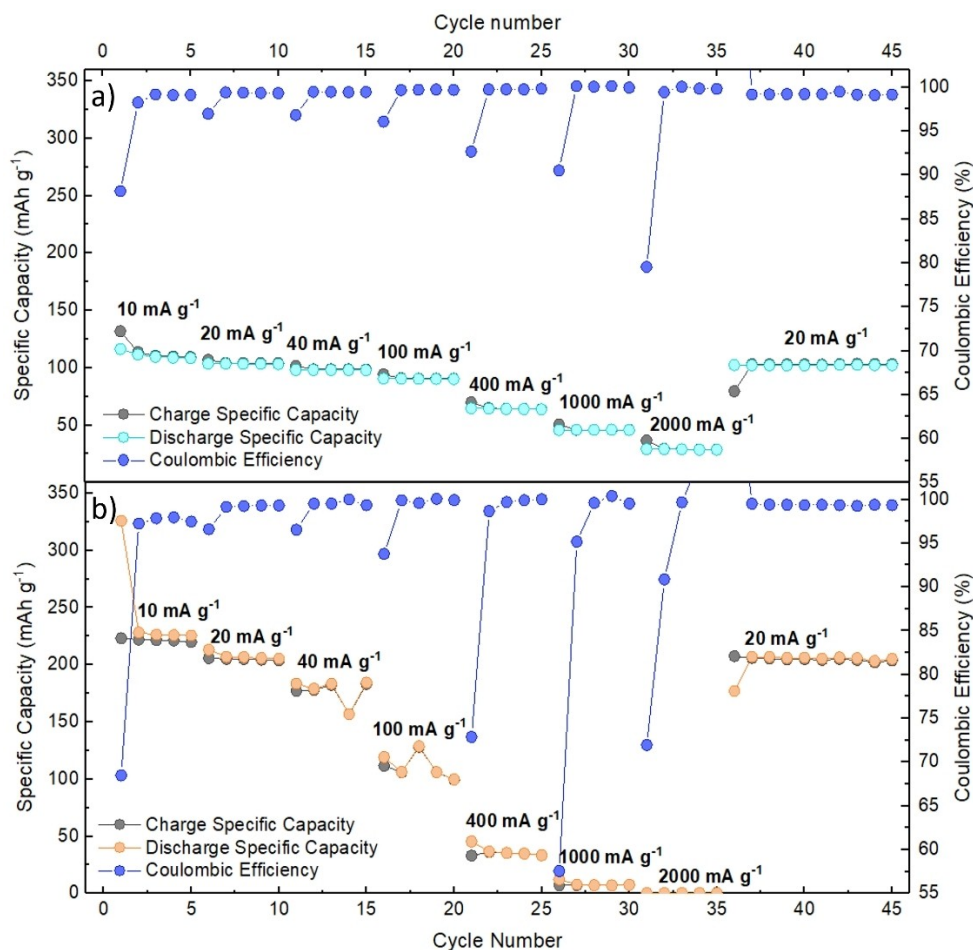


**Figure 1.** Rate capability of a) NaMnMO and b) CCDHC half-cells, indicating Cycle number vs. Specific capacity/Coulombic efficiency for each specific current applied.

material demonstrates its ability to withstand high specific currents by still maintaining a reversible capacity of  $29 \text{ mAh g}^{-1}$  at a current rate of  $2000 \text{ mA g}^{-1}$ . Upon restoring the specific current to  $20 \text{ mA g}^{-1}$ , the specific capacity fully recovers and remains at the same values as those previously obtained at the same rate, demonstrating excellent capacity recovery. Notably, coulombic efficiencies greater than 99.3% are observed after the first activation cycles for all tested current rates. From the related E vs. Q profiles, shown in Figure S5a, a low polarization of the material is displayed at all currents up to  $100 \text{ mA g}^{-1}$ , indicated by the sloping plateaus that only slightly shift to lower/higher potentials.

As for the CCDHC anode, at slow currents up to  $40 \text{ mA g}^{-1}$  the specific capacity only slightly decreases, while it becomes less stable at higher currents (Figure 1b). Especially when cycling at 1000 and  $2000 \text{ mA g}^{-1}$ , a drop in capacity and lower reversibility of the processes is observed, as indicated by the related coulombic efficiencies. Thus, the material shows a limited ability to sustain high specific currents. However, upon restoring a specific current of  $20 \text{ mA g}^{-1}$ , the specific capacity is fully recovered, and it stabilizes at values comparable to those previously observed for the same current rate. The related E vs. Q potential profiles in Figure S5b also show that the sloping

plateaus shift only slightly, indicating low polarization at all current densities up to  $40 \text{ mA g}^{-1}$ .

After testing the two materials separately in half-cells vs. Na metal at different current densities, their compatibility in full cell setup was evaluated. The electrodes were balanced by adjusting the mass loadings to obtain a negative-to-positive (N/P) charge ratio of 1.05–1.10, to prevent any Na-plating at the anode side. For the sake of clarity, the cell balancing was calculated without considering the contribution of the SEI formation at the first cycle, which would be compensated by the  $\text{Na}_2\text{C}_4\text{O}_4$  presodiation additive. In order to assess the influence of the FEC-containing electrolyte in absence of Na metal, two full cells were first compared. The results did not reveal any benefits in the use of electrolyte additives when in full cell configuration (refer to Figure S6 in the *Supporting Information* for further details). Hence, given the costly nature of the electrolyte solution when considering possible applications on a larger scale, the use of expensive FEC for all the tested full cells was hereby avoided.

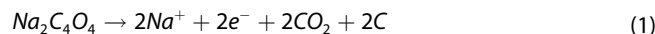
A long cycling for 120 cycles was performed by applying  $20 \text{ mA g}^{-1}_{\text{cat}}$  with two activation cycles at  $10 \text{ mA g}^{-1}_{\text{cat}}$  as this current density was the one yielding a better stability during the rate capability test. The working voltage window for the

CCDHC || NaMnMO full cell ( $1.20 \text{ V} < E < 4.29 \text{ V}$ ) was chosen by calculating the difference between the potential limits employed for the single half-cells. Figure 2 shows the trend of specific capacity upon cycling and the related E vs. Q profiles.

The CCDHC || NaMnMO full cell in Figure 2a shows an initial charge capacity of about  $138 \text{ mAh g}_{\text{cat}}^{-1}$ , which is in line with the first charge capacity of the bare NaMnMO when tested in half-cell configuration. A high irreversible capacity of  $53 \text{ mAh g}_{\text{cat}}^{-1}$  is observed upon the first discharge due to SEI formation/Na-ion trapping at the anode, resulting in a 60% initial coulombic efficiency, which is also in line with that displayed by the bare CCDHC when tested in half-cell configuration. As expected, after the irreversible processes during the first charge, the lack of an "infinite" source of sodium (i.e., the Na counter electrode in half-cells) results in charge unbalancing between the electrodes, with the cathode being only partly sodiated during the following discharge. This is more clearly visualized by considering the E vs. Q plot in Figure 2b, where the lower voltage cut-off of the cathode upon discharge is not reached. As a result, the cell is only able to deliver a specific capacity of about  $80 \text{ mAh g}_{\text{cat}}^{-1}$  after the first cycle. The coulombic efficiency quickly stabilizes at about

99.5% in the following cycles, meaning that a stable SEI is formed. However, the capacity slowly decreases up to  $36 \text{ mAh g}_{\text{cat}}^{-1}$  at the 120<sup>th</sup> cycle, with only a 46% capacity retention with respect to the third cycle, thus making the cell performance poorly suitable for practical applications.

To address the irreversible SEI formation/Na-ion trapping and increase the achievable specific capacity of the cell, sodium squarate ( $\text{Na}_2\text{C}_4\text{O}_4$ ) was chosen as a cheap and green sacrificial additive. Indeed,  $\text{Na}_2\text{C}_4\text{O}_4$  is thought to be decomposed during oxidation according to the reaction described by Equation (1), as generally reported in literature,<sup>[56]</sup> yielding a theoretical capacity of  $339 \text{ mAh g}^{-1}$ .



To calculate the amount of salt needed to compensate for the sodium loss during the first cell charge,<sup>[56]</sup> electrodes only based on  $\text{Na}_2\text{C}_4\text{O}_4$  as the active material were prepared. The irreversibility of the process and the specific capacity provided upon salt oxidation, was studied by means of CV at a scan rate of  $0.1 \text{ mV s}^{-1}$  and galvanostatic cycling at a C-rate of C/10 (Figure S7). From the CV measurement in Figure S7a, a single

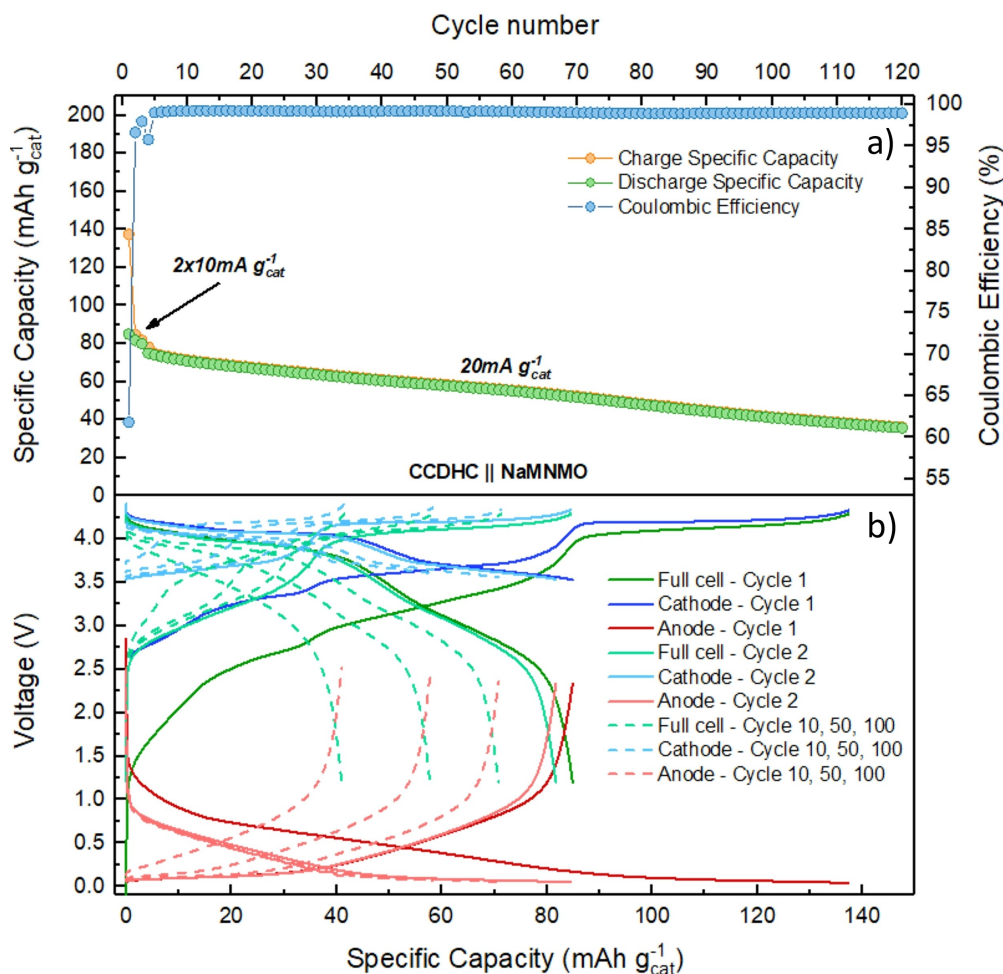


**Figure 2.** a) Galvanostatic cycles and b) E vs. Q potential profiles obtained at  $20 \text{ mA g}_{\text{cat}}^{-1}$  current density with two activation cycles at  $10 \text{ mA g}_{\text{cat}}^{-1}$  for the full cell CCDHC || NaPF<sub>6</sub> in EC:PC || NaMnMO. The applied current densities and specific capacities are normalized according to the mass of the cathode active material. The cathode and anode potentials (blue and red, respectively) are referred to the Na<sup>+</sup>/Na redox couple.

oxidation peak centered at about 3.75 V is observed at the first charge, which is related to the squarate decomposition, as reported in literature.<sup>[55]</sup> After the first oxidation, no other process is displayed, indicating a fully irreversible salt decomposition. From the galvanostatic cycling in Figure S7b, the specific capacity normalized to the amount of  $\text{Na}_2\text{C}_4\text{O}_4$  in the electrode is calculated to be  $315 \text{ mAh g}^{-1}$ , which is very close to the theoretical capacity of the salt ( $Q_{\text{th}} = 339 \text{ mAh g}^{-1}$ ).

By knowing the amount of charge provided by  $\text{Na}_2\text{C}_2\text{O}_4$  and the charge needed to address the irreversible losses at the anode during the first charge, electrodes of NaMnMO-SSq with the proper amount of sodium squarate in the formulation (23.28%) were fabricated and tested in half-cell configuration. The effect of  $\text{Na}_2\text{C}_4\text{O}_4$  on the cyclability of the cathode material and on the reversibility of the redox processes was first investigated by means of CV, as shown in Figure 3.

The voltammograms in Figure 3a show the typical NaMnMO redox processes (i.e., peaks A and B) associated with the  $\text{Ni}^{2+}/\text{Ni}^{3+}$  and  $\text{Ni}^{3+}/\text{Ni}^{4+}$  oxidations, respectively. An additional feature between 3.6 V and 4.1 V (peak S), which is not repeated in the following cycles, is also observed, consistent with the irreversible squarate decomposition; during the cathodic scans, no reduction peak for the process associated with peak S is observed, while the reductions of  $\text{Ni}^{4+}$  to  $\text{Ni}^{3+}$  and eventually back to  $\text{Ni}^{2+}$  (i.e., peaks B' and A', respectively) are clearly visible. The signal related to the P2-to-OP4 phase transition (peak C) is barely visible during the anodic scan, as well as the signal associated with the reverse process (peak C') in the subsequent cathodic scan, suggesting that the phase transition is not started. Generally, all signals in the CV are highly polarized, especially after the irreversible decomposition of  $\text{Na}_2\text{C}_4\text{O}_4$ . When comparing the CV of NaMnMO with that of NaMnMO-SSq (Figure 3b), the processes are only superimposed during the first charge until 3.65 V. After the decomposition of

sodium squarate, all the following redox processes seemingly become polarized. Moreover, after the first cycle, the shape of the peaks changes and becomes broader as compared to those of NaMnMO, with peaks C/C' completely disappearing after the first cycle, thus indicating a change in the redox activity of the cathode material.

To further investigate the effect of sodium squarate on the charge/discharge performance and stability of the cathode material, NaMnMO-SSq half-cells vs. Na were galvanostatically cycled in the same conditions as the bare NaMnMO electrodes ( $2.70 \text{ V} < E < 4.30 \text{ V}$  potential window,  $20 \text{ mA g}^{-1}$  specific current, with two activation cycles at  $10 \text{ mA g}^{-1}$ ). The specific capacity and related coulombic efficiency upon cycling are reported in Figure 4.

The initial charge capacity of NaMnMO-SSq is higher than  $180 \text{ mAh g}^{-1}$ , as shown by the galvanostatic cycling in Figure 4a, indicating that the  $\text{Na}_2\text{C}_4\text{O}_4$  additive successfully provided additional sodium upon oxidation. However, after the slow activation cycles, the specific capacity drops to  $60 \text{ mAh g}^{-1}$ , which is lower than the reversible capacity of bare NaMnMO when used in full cell with CCDHC. Within 45 cycles, the capacity retention upon cycling is 75% (the third cycle is here considered as a reference), with the coulombic efficiency slowly rising to values higher than 95% and eventually stabilizing at values close to 99%. Figure 4b–c shows the potential profiles and related differential plots that confirm the observations made in Figure 3 from the CV analyses. The irreversible squarate decomposition is clearly distinguishable at the first cycle, with all processes in the following cycles displaying a very high polarization, and a decrease in specific capacity as the phase transition plateaus/peaks disappear. The oscillations in voltage profiles, particularly in the initial cycles, can be attributed to polarizations caused by  $\text{CO}_2$  evolution.

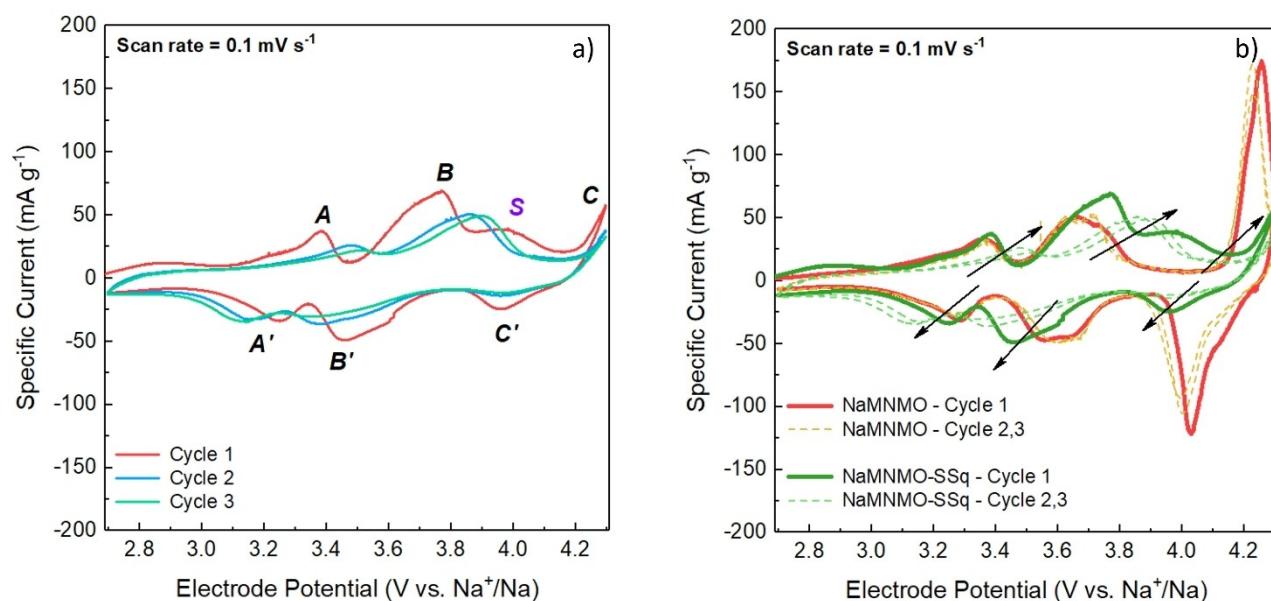


**Figure 3.** a) Cyclic voltammetry of the first three cycles at a scan rate of  $0.1 \text{ mV s}^{-1}$  for NaMnMO-SSq and b) Comparison between the redox peaks in NaMnMO and in NaMnMO-SSq half-cells at the same scan rate.

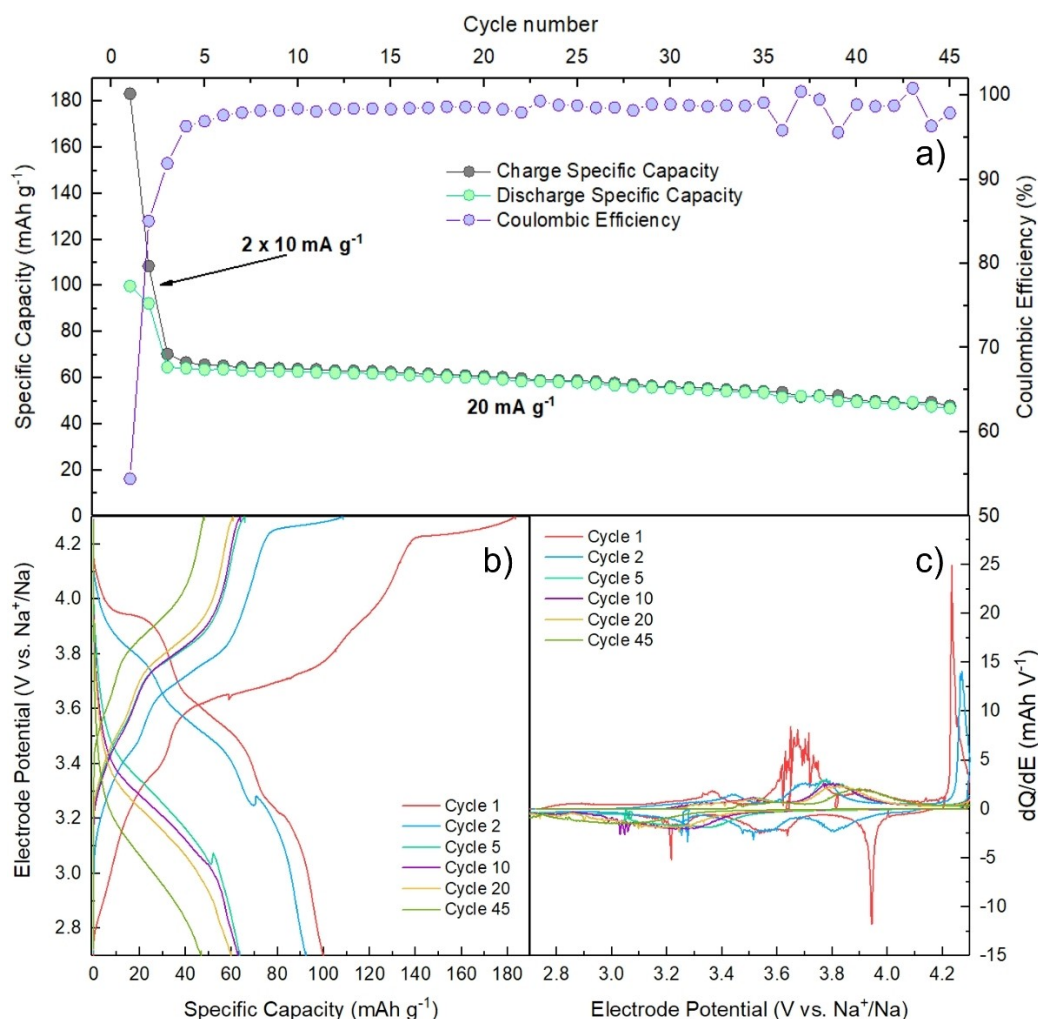


**Figure 4.** Galvanostatic cycles obtained at 20 mA g<sup>-1</sup> current density with two activation cycles at 10 mA g<sup>-1</sup> for NaMnMO-SSq half-cell: a) Cycle number vs. Specific capacity/Coulombic efficiency; b) E vs. Q potential profiles; c) Differential dQ/dE vs. E profile.

The behavior of the NaMnMO-SSq cathode was also evaluated in full cell configuration, by cycling the cell at a current density of 20 mA g<sup>-1</sup><sub>cat</sub> for 120 cycles with two activation cycles at 10 mA g<sup>-1</sup><sub>cat</sub> (Figure 5).

The CCDHC || NaMnMO-SSq full cell (Figure 5a) displays an initial charge capacity of about 200 mA h g<sup>-1</sup><sub>catr</sub> in line with the first charge capacity of the presodiated cathode tested in half-cell configuration. Upon discharge at the first cycle, a high irreversible capacity of 60 mA h g<sup>-1</sup><sub>cat</sub> is observed due to SEI formation/Na trapping at the anode. This irreversible capacity corresponds to an initial coulombic efficiency of about 55%, which is consistent with the initial coulombic efficiency observed for the CCDHC half-cell. The specific capacity in the subsequent cycles stabilizes at values of about 90–95 mA h g<sup>-1</sup><sub>catr</sub> thus demonstrating an improvement as compared to the full cell CCDHC || NaMnMO shown in Figure 2. However, after the first 15 cycles the cell capacity decreases with a progressive charge unbalancing, as indicated by the cut-off voltage slippage of anode and cathode upon cell discharge (Figure 5b). The redox processes associated to the cathode, especially at high voltage, are also affected becoming more and more polarized.

When considering the first 40 cycles (Figure 4c), our results show that the CCDHC || NaMnMO-SSq full cell still outperforms the NaMnMO || CCDHC one, and the coulombic efficiency slowly stabilizes to average values of about 99%, consistently with data reported in literature for similar materials.<sup>[59]</sup> However, upon longer cycling (Figure 5d), the specific capacity becomes comparable to that of the CCDHC || NaMnMO full cell after about 70 cycles, maintaining a similar descending trend up to 120 cycles. A final capacity of 40 mA h g<sup>-1</sup><sub>cat</sub> and a capacity retention of 44% with respect to the third cycle are recorded at the 120<sup>th</sup> cycle. When comparing the coulombic efficiencies between the two cells, some fluctuations are also encountered in the presodiated full cell upon long-term cycling. Interestingly, these results clearly show that there are still limitations to be overcome when using presodiation additives under more practical conditions than those commonly explored in the literature (i.e., P2-type cathodes entering high voltage regions, prolonged cycling and high electrode mass loadings).

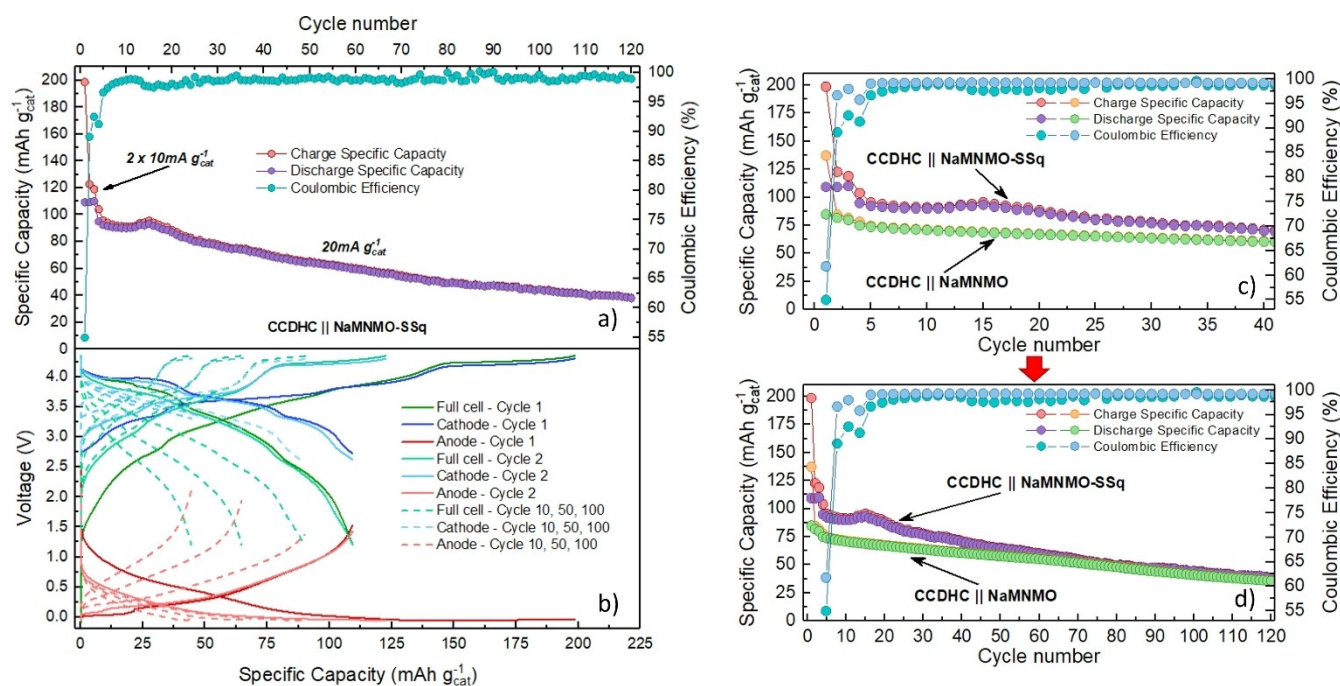


**Figure 5.** a) Galvanostatic cycles and b) E vs. Q potential profiles obtained at  $20 \text{ mA g}^{-1}_{\text{cat}}$  current density with two activation cycles at  $10 \text{ mA g}^{-1}_{\text{cat}}$  for the full cell CCDHC || NaMnMO-SSq; Performance comparison between CCDHC || NaMnMO and CCDHC || NaMnMO-SSq c) within the first 40 cycles and d) upon long cycling up to 120 cycles. The applied current densities and specific capacities are normalized according to the mass of the cathode active material. The cathode and anode potentials (blue and red, respectively) are referred to the  $\text{Na}^+/\text{Na}$  redox couple.

### Morphological, Structural and Interfacial Evolution

To further understand the role of the presodiation additive in the full cell, the morphological, structural, and interfacial evolutions of the materials were investigated by means of intermittent SEM, *operando* XRD, synchrotron XAS, *ex-situ* XPS, and impedance spectroscopy.

In Figure S8 and Figure 6, the change in surface morphology of NaMnMO and NaMnMO-SSq during the first desodiation in the full cell has been evaluated.

No substantial differences in terms of morphology can be identified between the pristine (Figure S8a,c,e) and the desodiated (Figure S8b,d,f) NaMnMO electrode, even at higher magnifications and in all the sampling spots considered. Apart from the formation of some cracks on the electrode surface after desodiation, the electrode surface and particle morphology stay unchanged. Unfortunately, further investigations beyond the first desodiation were not possible with intermittent SEM, as both NaMnMO and NaMnMO-SSq electrodes underwent delamination from the current collector.

When considering NaMnMO-SSq, the surface morphology for all the observed locations in the desodiated electrode (Figure 6b,d,f) displays several differences as compared to the pristine one (Figure 6a,c,e). After the first charge, the surface texture of the electrode shows the formation of several holes, likely due to the decomposition of  $\text{Na}_2\text{C}_4\text{O}_4$ . For the sake of clarity, micrographs obtained in the same sampling zone at lower magnifications, before and after the first desodiation, are provided in Figure S9 to show the homogeneous formation of

these surface features, hence confirming the homogeneous dispersion of the presodiation additive within the electrode mixture. The resulting increase in electrode porosity may improve ion transfer and reaction kinetics, and depending on their shape, holes may also be relevant during later cycles. Under these conditions, the electrode is under tension and cracks may nucleate at the edges or corners of the holes. Since holes are located within the carbon black/binder regions, this possible damage will most likely not severely affect the active material. However, for long-term performance, such cracks can be detrimental (so-called "chemomechanical fatigue").<sup>[73]</sup> The large crack around the active material in Figure 6e,f is most likely due to shrinkage of the carbon black/binder domain caused by the decomposition of  $\text{Na}_2\text{C}_4\text{O}_4$ . Large gaps/trenches, such as the one shown in Figure 6f, may lead to electrical disconnections of active particles, causing a faster decrease in long-term performance. Based on these findings, it can be expected that a limited content of the additive and a homogeneous distribution of small  $\text{Na}_2\text{C}_4\text{O}_4$  particles are beneficial for the retention of the electrical contacts within the electrode after the decomposition of the additive.

To better understand the different electrochemical behavior upon presodiation, a detailed study of the structural evolution upon cycling was carried out for both NaMnMO and NaMnMO-SSq by means of *operando* XRD, performed during the first two cycles of each material. The obtained diffraction patterns, which correspond to the specific electrode potential, are reported in Figure S10 and Figure 7.

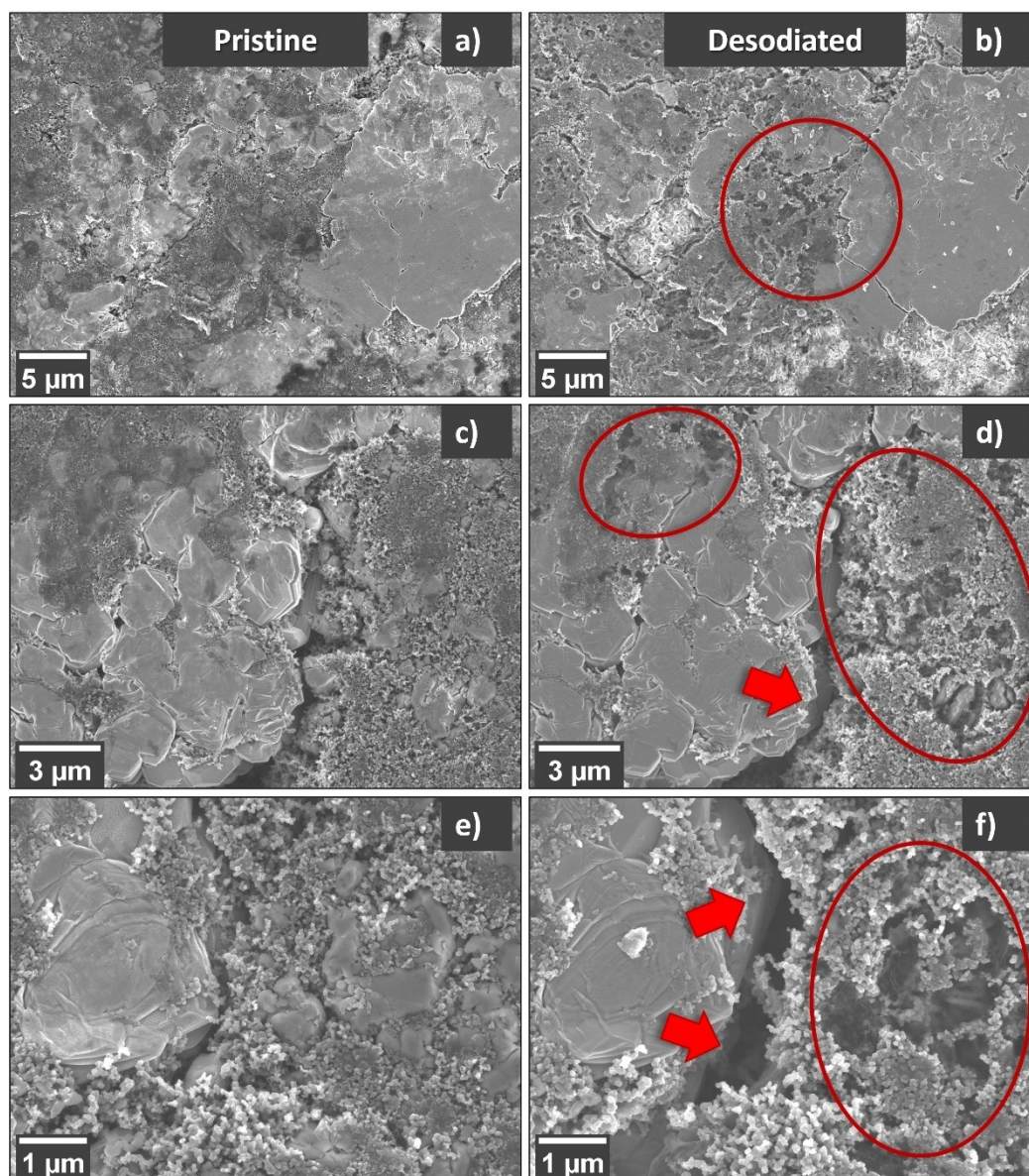


**Figure 6.** SEM micrographs of NaMnMO-SSq electrode at different magnifications and in different spots: a), c), e) pristine electrode before cycling and b), d), f) same sampling zones after the first desodiation inside a full cell. Circles indicate the formation of holes and arrows indicate cracks enlargement.

Before any electrochemical process takes place (i.e., at OCV), all reflections of NaMnMO perfectly match those obtained from the pristine powder in Figure S1a, consistently with works reported in literature.<sup>[60,63]</sup> Upon cycling within the  $2.7\text{ V} < E < 4.3\text{ V}$  potential window, several structural changes are observed for the NaMnMO half-cell (Figure S10), consistently with the electrochemical profiles. In the high-voltage plateau region, it is possible to observe the formation of the Z-phase during oxidation, which is reversibly converted to the initial P2 phase upon subsequent reduction thanks to the structural stabilization provided by Mg doping.<sup>[62,74–78]</sup> A more detailed description of the phase transitions occurring in NaMnMO can be found in the *Supporting Information* file.

When considering the NaMnMO-SSq half-cell (Figure 7), the structural evolution upon cycling displays a rather different

behavior, with both the  $a$  and  $c$  lattice parameters only changing at the beginning of the first charge and until the decomposition of squarate, after which they remain basically constant. When reaching  $3.9\text{ V}$ , the 002 reflection only shows a slight shift back to higher angles, before going back to lower diffraction angles and then remaining constant throughout the whole cycling. This trend in the  $c$ -parameter indicates that, especially during  $\text{Na}_2\text{C}_4\text{O}_4$  decomposition upon the first charge, the structure of the material does not change largely. Moreover, the Z-phase is never reached, indicating a polarization or suppression of the phase transition. The lack of a flat plateau in the high-voltage region as compared to NaMnMO may indicate that the  $\text{Na}^+$ /vacancy ordering is prevented for NaMnMO-SSq. This effect generally results in alleviated oxygen layer gliding, increased  $\text{Na}^+$  diffusion coefficient and delayed/suppressed

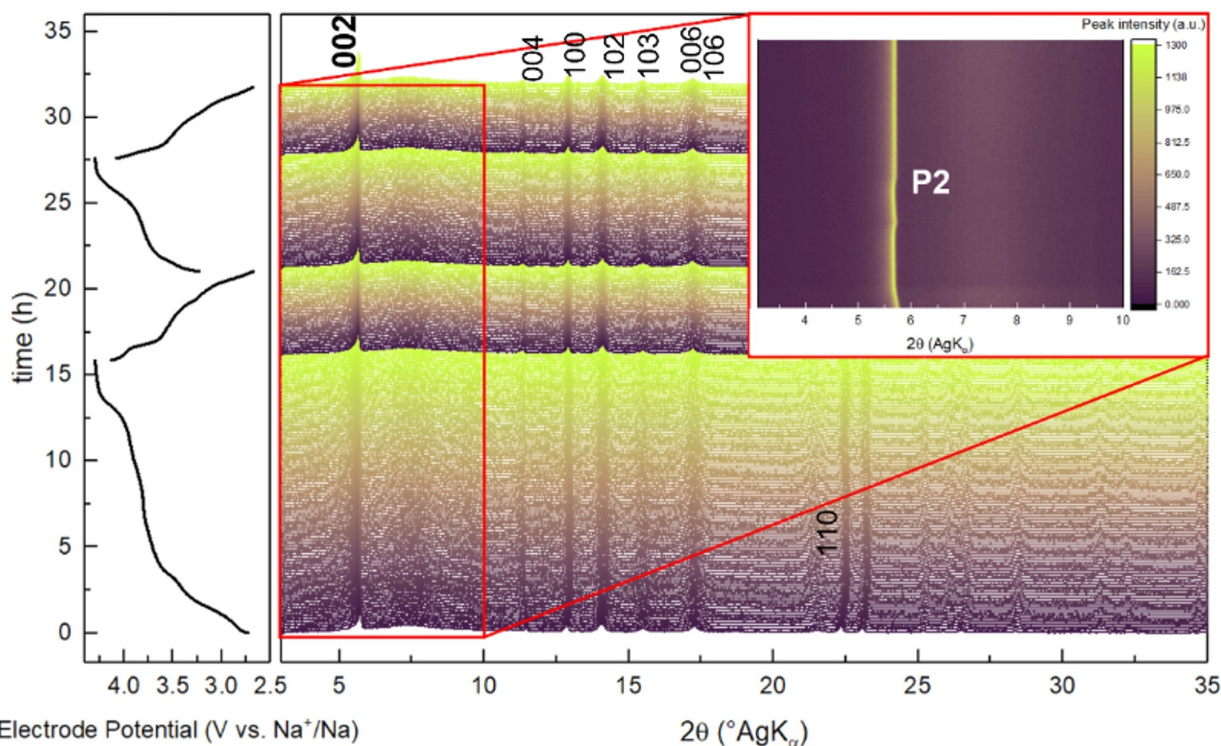


**Figure 7.** Operando XRD performed upon the first two cycles at  $10 \text{ mA g}^{-1}$  for NaMnMO-SSq half-cell. The inset shows a contour map highlighting the 002-reflection region associated to the P2 phase.

phase transformations.<sup>[19,78]</sup> It was also recently reported that a higher sodium content could allow the structure to maintain a higher amount of  $\text{Na}^+$  ions within the interlayers when the same amount of Na is deintercalated, preventing irreversible structural transitions (e.g., P2-to-O2 transition).<sup>[79]</sup> Ultimately, a polarization of the signal due to gas formation or parasitic reactions involving Ni ions and electrolyte decomposition, cannot be excluded.<sup>[62]</sup> Nevertheless, being the P2  $\rightarrow$  Z-phase transformation suppressed/polarized, a loss of capacity from the related high-voltage region is observed. The better initial performance displayed by NaMnMO-SSq in terms of specific capacity can possibly be associated to the  $\text{Na}^+$ /vacancy disordering providing a better diffusion. However, the stabilization effect of Mg-doping might be negatively affected, as the capacity retention in the long-term cycling is worsened.

The evolution of the oxidation state and variations in the Mn and Ni local environments during the first cycle of NaMnMO and NaMnMO-SSq half-cells were monitored by means of synchrotron X-ray absorption spectroscopy (XAS). The galvanostatic profiles, highlighting the acquisition points for both transition metals, are presented in Figure S11.

The XAS data obtained for NaMnMO and NaMnMO-SSq have been compared to the standard references Mn,  $\text{MnO}$ ,  $\text{Mn}_2\text{O}_3$ ,  $\text{MnO}_2$ , Ni and NiO, in order to define the oxidation state and chemical coordination environment of the metal ions during cycling. The X-ray absorption near edge structure (XANES) spectra at the Mn K-edge (Figure S12a,b) are consistent with Mn always staying in +4 oxidation state for both NaMnMO and NaMnMO-SSq, as no relevant shifts are observed

during charge/discharge. The extended X-ray absorption fine structure (EXAFS) spectra in Figure S12c,d further confirms this result, with the interatomic distances in the Mn local environment never changing for both NaMnMO and NaMnMO-SSq. This confirms that the tetravalent Mn ions stay electrochemically inactive within the cycling conditions employed, providing stabilization to the structure as observed for similar doped materials,<sup>[80–82]</sup> and are not affected by the decomposition of  $\text{Na}_2\text{C}_4\text{O}_4$ .

Concerning the Ni ions in the structure, the XANES spectra in Figure 8a,b show that the pristine electrodes are consistent with Ni being in +2 oxidation state. Upon charge, the Ni K-edge of NaMnMO shifts to higher energy regions as a result of  $\text{Ni}^{2+}$  oxidation. An energy shift of about 4 eV is observed when going from OCV to the charged state up to 4.3 V, which is consistent with the oxidation of Ni up to +4 oxidation state [83,84]. Interestingly, the oxidation of Ni to +4 oxidation state is still observed for NaMnMO-SSq (4 eV energy shift when going from OCV to the charged state) despite the absence of phase transitions in the high-potential region, as displayed in Figure 7. When comparing the spectra of the two cathodes, the energy shift in NaMnMO occurs gradually during the whole charge, while NaMnMO-SSq displays a more sudden shift to higher energies when squarate is decomposing ( $E > 3.7 \text{ V}$ ), as shown in the insets of Figure 8a,b. This result suggests that, while in NaMnMO the Ni charge transfer reaction spans throughout the whole charging process, in NaMnMO-SSq there is a jump in the redox activity of Ni taking place in the high-voltage region, in correspondence of the squarate decomposition. The Ni EXAFS

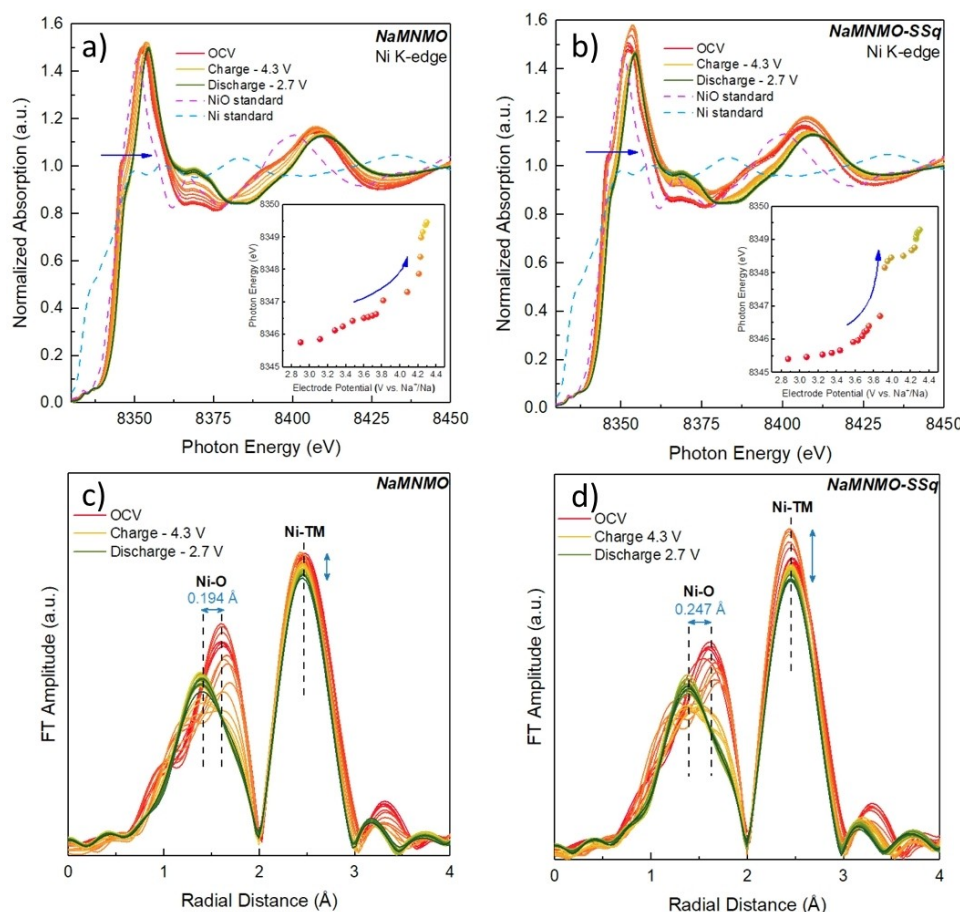


**Figure 8.** XANES spectra at Ni K-edge for a) NaMnMO and b) NaMnMO-SSq; corresponding EXAFS spectra for c) NaMnMO and d) NaMnMO-SSq. The insets in panels a) and b) show the photon energy shift as a function of potential. The colors for the spectra at different potentials correspond to those indicated in the galvanostatic profiles (see Figure S11).

results are reported in Figure 8c,d, showing the characteristic shells at 1.6 Å and 2.6 Å, related to the Ni–O and Ni–TM coordination, respectively. Upon charge, the Ni–O interatomic distance decreases because of Ni oxidation, with progressive changes in the Ni–O shell shape confirming a progressive transition from Ni<sup>2+</sup> to Ni<sup>4+</sup>.<sup>[80–82]</sup> As for the Ni–TM interatomic distances, they are comparable to those of Mn–TM shown in Figure S12c,d, suggesting that Ni and Mn ions are randomly and uniformly distributed in the TM layer.<sup>[85]</sup>

Upon discharge, the XANES and EXAFS results for both NaMnMO and NaMnMO-SSq indicate that the Ni K-edge and Ni–O interatomic distance do not completely go back to the initial stage. The partial irreversibility of these signals during the first cycle may account for some lattice oxygen irreversibly contributing to capacity in the high-voltage region.<sup>[86,87]</sup> Nevertheless, by considering only Ni<sup>2+</sup>/Ni<sup>4+</sup> as the redox-active couple in NaMnMO, an achievable theoretical capacity of 105 mAh g<sup>−1</sup> (0.4 Na<sup>+</sup> equivalents) can be calculated, which is in good agreement with its practical capacity (Figure 1a) and confirms the oxidation of Ni<sup>2+</sup> to Ni<sup>4+</sup>. Interestingly, the Ni–O bond length for NaMnMO recovers more reversibly to the initial position after discharge, supporting its higher cycling stability as compared to NaMnMO-SSq. Moreover, peak amplitudes in

NaMnMO-SSq decrease more pronouncedly, especially for the Ni–TM bonds. Hence, it is reasonable to assume that after the first electrochemical cycle the material is prone to a partially irreversible local structural deformation.<sup>[80]</sup>

In order to obtain more insights into the different behavior of the two full cells, the composition of the passivation layers at the cathode and anode after the first cycle was investigated. Indeed, when opening the cycled cells, differences in the electrolyte decomposition products were already observed, as the separators employed in the presodiated full cell displayed a much brownish color on the anode side, thus possibly indicating a more severe electrolyte decomposition as displayed in Figure 9a. Hence, the chemical composition of SEI/CEI after the first cycle was examined in detail by means of *ex-situ* XPS. The C1s spectra of NaMnMO and CCDHC electrodes analyzed in pristine conditions as well as after 1 cycle, with and without the squarate additive, are reported in Figure 9b–c.

When considering the cathode side (Figure 9b), the pristine NaMnMO electrode shows the presence of four peaks: the sp<sup>2</sup> hybridized carbon from the Super C-65 conductive additive at ~284.4 eV; the signal at 285 eV is assigned to sp<sup>3</sup>-C hydrocarbon (–C–H) species (i.e. adventitious carbon); the two chemical environments of the polyvinylidene fluoride (PVdF) binder,

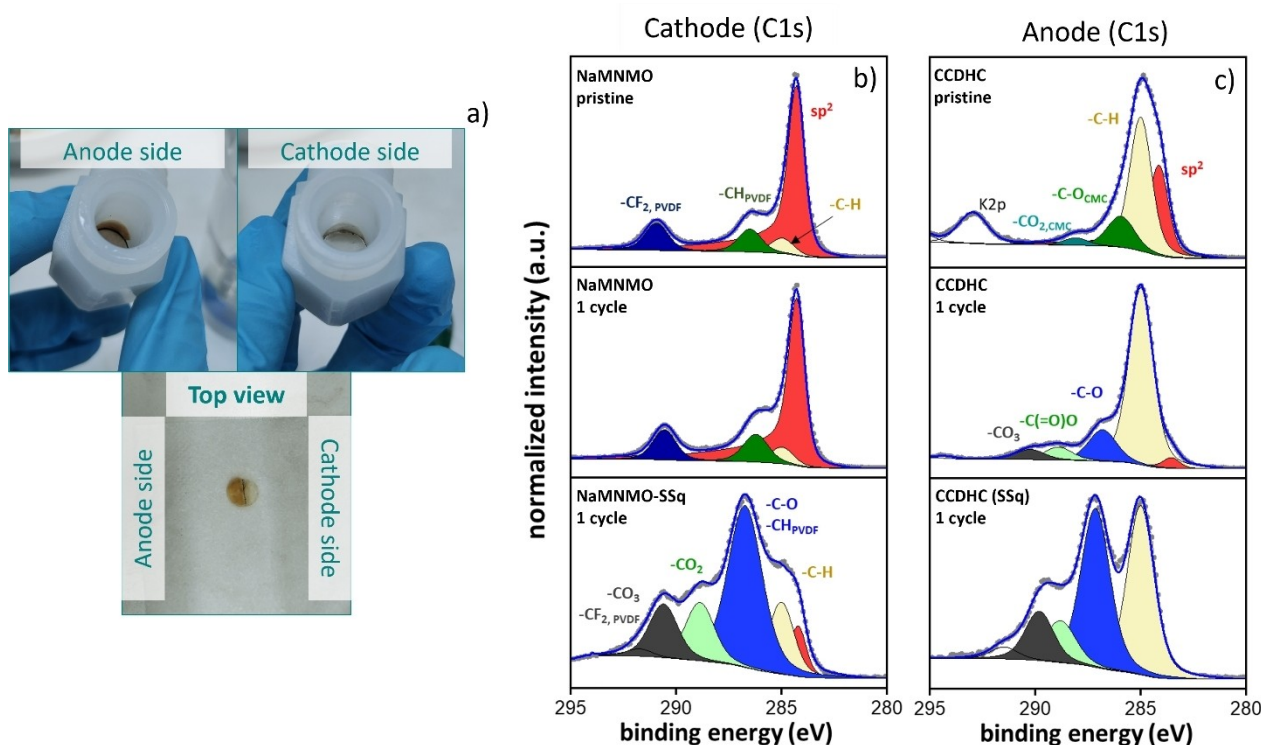


**Figure 9.** a) Picture of the top-side separator after cycling of CCDHC || NaMnMO-SSq full cell; C1s XPS spectra of b) NaMnMO and c) CCDHC electrodes in pristine conditions as well as after one cycle in full cell, with and without the presence of squarate.

-C-H at 286.5 eV, and -C-F at 290.9 eV, respectively.<sup>[88,89]</sup> After one cycle, the NaMnMO electrode displays a similar composition, indicating a low electrolyte degradation. By contrast, the addition of squarate to the electrode yields intense peaks corresponding to the formation of ethers, -C-O (286.8 eV), as well as ester, -CO<sub>2</sub> (288.8 eV), and carbonates, -CO<sub>3</sub> (290.5 eV), within the Cathode Electrolyte Interphase (CEI). Interestingly, the decomposition of SSq leads to an about 5-fold increase in the atomic concentration of -C-O ether species (from 4.6 at.% to 22.7 at.%) and the corresponding O1s spectra, both provided in the *Supporting Information* (Table S1 and Figure S13a). As for the presence of -CO<sub>3</sub> and -CO<sub>2</sub> species, they are most likely the result of reactions of gaseous CO<sub>2</sub> at the electrode interfaces. As the fluorine content is found to be lower in the NaMnMO-SSq electrode as compared to NaMnMO (Table S1 and Figure S14a), we also suspect that a lower amount of NaPF<sub>6</sub> salt from the electrolyte is decomposed in favor of a more ether- and carbonate-rich interphase. In addition, the intensity of the *sp*<sup>2</sup> peak strongly decreases in NaMnMO-SSq as compared to NaMnMO. This behavior suggests that the presence of the squarate additive causes the formation of a thicker electrode-electrolyte interphase, as the growing thickness of the interfacial layer partially masks the *sp*<sup>2</sup> signal coming from elemental carbon.

As for the anode side (Figure 9c), the pristine CCDHC electrode also displays four main peaks: the *sp*<sup>2</sup> hybridized hard carbon at ~284.2 eV; the -C-H signal from hydrocarbons at 285 eV; the two chemical environments of the carboxymethyl cellulose (CMC) binder, -C-O-C- at 286.5 eV and -CO<sub>2</sub> at

288.3 eV, respectively.<sup>[88,89]</sup> After one cycle in the CCDHC || NaMnMO cell, a strong decrease in the *sp*<sup>2</sup> signal from the hard carbon is observed, with the disappearance of the CMC chemical environments and an increase in the intensity of hydrocarbon species. Ether -C-O (286.7 eV), ester -CO<sub>2</sub> (288.9 eV), and carbonate -CO<sub>3</sub> (290.1 eV) species are emerging, resulting from the decomposition of EC and PC to form the SEI layer. The addition of squarate leads to further thickening of the SEI layer, as all three major SEI components (i.e., -C-O, -CO<sub>2</sub>, and -CO<sub>3</sub>) increase in intensity and completely mask the *sp*<sup>2</sup> peak of elemental carbon underneath. Interestingly, even though the SEI layers of SSq-free and SSq-containing cells differ in terms of absolute atomic weight fractions, it is observed that the relative atomic weight fractions of -CO<sub>2</sub> species did not change significantly between NaMnMO-SSq and NaMnMO after one cycle and the -CO<sub>3</sub> species only increased slightly (from 3.0 at.% to 5.6 at.%). In terms of relative changes, the C-O component displayed the most significant increase. The fact that the carbon contents are similar in their relative amounts is due to the correlated increase in oxygen content of surface layers formed in presence of SSq (Table S1 & Figure S13b). Finally, as seen in the spectra for NaMnMO, the fluorine content decreased as a result of surface layer formation by about 5 at.% (Table S1 & Figure S14b).

By combining these results with those obtained for the cathodes, several considerations can be made: (I) the CEI and SEI compositions change considerably in presence of SSq, as indicated by the relative peak intensities in the C1s spectra; (II) after SSq decomposition, the main surface components at both

electrodes are -C-O species (ethers); (III) accordingly, the presence of SSq generally lead to a considerable increase of the oxygen content in the surface layers; (IV) the F-content is lower for both electrodes of the CCDHC || NaMnMO-SSq cell after the first cycle, suggesting less electrolyte salt decomposition and inclusions but also coverage of the fluoride-containing binder in the inner surface layer.

Although these measurements alone cannot provide an exact understanding of how the presodiation occurs and how the degradation mechanism proceeds, based on the obtained results it is reasonable to assume that, in this system, the decomposition of squarate is a much more complex process than Equation (1) suggests. Specifically, the differences in the C-content between anode and cathode can be rationalized by the different gas concentrations at the electrodes, as the cathode side (where the CO<sub>2</sub> is generated) is likely to be the electrode where most of the reactions occur. Most importantly, the decomposition products at the electrodes' surface indicate the presence of thicker interphases in the CCDHC || NaMnMO-SSq cell, with a higher amount of ether-based organic species possibly leading to the formation of more insulating passivation layers.

To further investigate the interfacial properties of the materials, impedance spectra were recorded in full cell configuration at the bias potential of 4.0 V during the 1<sup>st</sup> and 2<sup>nd</sup> cycle, and then every 12<sup>th</sup> cycle upon charge (Figure 10), using a three-electrode cell setup with Na metal ring reference (EL-CELL). The obtained Nyquist plots (Figure 10a–b) are characterized by five main features: (I) an intercept with the real axis in the high frequency region; (II) a small semicircle at high frequencies; (III) a semicircle in the medium frequency region; (IV) a semicircle in the medium-to-low frequency region; (V) a straight line in the low frequency region. The Nyquist plots have been modeled by the Equivalent Circuit method,<sup>[90]</sup> and the related parameters have been calculated through a non-linear least-squares (NLLS) fitting protocol by using the RelaxS3 software (rhd instruments). The intercept (I) at high frequencies represents the migration of Na<sup>+</sup> ions through the electrolyte solution, and it was modeled as a pure resistive element (R<sub>el</sub>). The first small semicircle (II) at high frequencies is attributed to the contact resistance between the current collector and the electrode particles, and modeled as a resistive element (R<sub>cont</sub>) in parallel with a double-layer capacitive element (C<sub>cont</sub>). The semicircle (III) at medium frequencies is related to the migration of Na<sup>+</sup> ions through the passivation layers of the anode and cathode with charges accumulating onto their surface, and was modeled as a resistive element (R<sub>SEI/CEI</sub>) in parallel with a capacitor element (C<sub>SEI/CEI</sub>). The bigger semicircle (IV) at medium-to-low frequencies can be ascribed to the faradaic charge transfer process with double layer formation onto the surface of the active material particles, modeled as a resistive element (R<sub>ct</sub>) in parallel with a capacitor element (C<sub>dl</sub>). Finally, the line (V) at low frequency describes a semi-infinite diffusion to a blocking electrode, which was modeled with a Warburg impedance (W), in series with a capacitor element (C<sub>i</sub>) indicating intercalation capacitance. The resulting equivalent circuit, written according to Boukamp's notation,<sup>[91,92]</sup> is  $R_{el}(R_{cont}C_{cont})(R_{SEI/CEI}C_{SEI/CEI})$

$(R_{ct}C_{dl})WC_i$ . For the fitting procedure, the pure capacitive elements were substituted by constant phase elements (Q), in order to consider the non-ideal, capacitive behavior given by electrode inhomogeneity and surface roughness.<sup>[90]</sup> To better visualize and deconvolute all impedance contributions, the DRT analysis method was applied, by calculating the function  $\gamma$  according to Tikhonov regularization [93,94] (Figure 10e–f). The low frequency points, as simulated by WC<sub>i</sub> elements, were subtracted from the overall impedance (Figure 10c–d).

The Nyquist plots obtained after Warburg subtraction for the two full cells upon cycling are shown in Figure 10c–d, and the fitting has been performed by using the equivalent circuit  $R_{el}(R_{cont}C_{cont})(R_{SEI/CEI}C_{SEI/CEI})(R_{ct}C_{dl})$ . After subtraction, all semicircles and their evolution are better visible, especially the low-frequency semicircle. In particular, a huge difference can be observed in the magnitude of the resistances between the two cells, as the CCDHC || NaMnMO system displays much lower polarizations with respect to the presodiated CCDHC || NaMnMO-SSq system. From the calculation of the DRT (Figure 10e–f), all polarizations associated with the related semicircle from the Nyquist plot can be better deconvoluted according to their different time constants, thus resulting in different characteristic frequencies.<sup>[95]</sup> A complete separation of the single contributions from the anode and cathode was not possible due to their time constants being too close to each other. However, when plotting the DRT as a function of cycle number it was possible to define three main contributions for each cell (the small hump at low frequencies, labeled as \*, is an artifact due to the removal of the Warburg diffusion). The peak labeled as P1 in the high frequency range is small and constant throughout cycling, hence it is consistent with the contribution of the contact resistance (R<sub>cont</sub>). Peak P2 in the high-to-medium frequency range can be related to the sum of the resistances of the passivation layers for both electrodes (R<sub>SEI/CEI</sub>), with the R<sub>SEI</sub> being the dominant polarization. As for peak P3 in the low-frequency region, it displays the strongest dependency on the number of cycles and it increases in both cases, hence it is associated with the resistance of charge-transfer (R<sub>ct</sub>) of both electrodes upon cycling. Interestingly, the trend of the polarizations is the same in both cells, with P3 continuously increasing and P2 remaining constant after the first cycles. By comparing the peak intensities, both P2 and P3 in CCDHC || NaMnMO-SSq are much higher than in CCDHC || NaMnMO, indicating a greater polarization from both the passivation layer and the charge transfer, as observed from the Nyquist plots. The different shifts of the peak frequencies between the two systems upon cycling, summarized in Table S2, further support these assumptions. Indeed, peak P2 in CCDHC || NaMnMO is initially centered between 10 and 100 Hz, and it undergoes a progressive peak shift towards higher frequencies upon cycling (f ~100 Hz, cycle 92). This indicates a progressive stabilization of the interphases and a faster kinetics after their formation. This effect is much less evident in CCDHC || NaMnMO-SSq, where P2 is initially centered between 1 and 10 Hz and only slightly shifts to higher frequencies (f ~10 Hz, cycle 92), indicating a slower transport kinetics, as expected from the formation of thicker interphases. As for the charge transfer process, P3 is initially

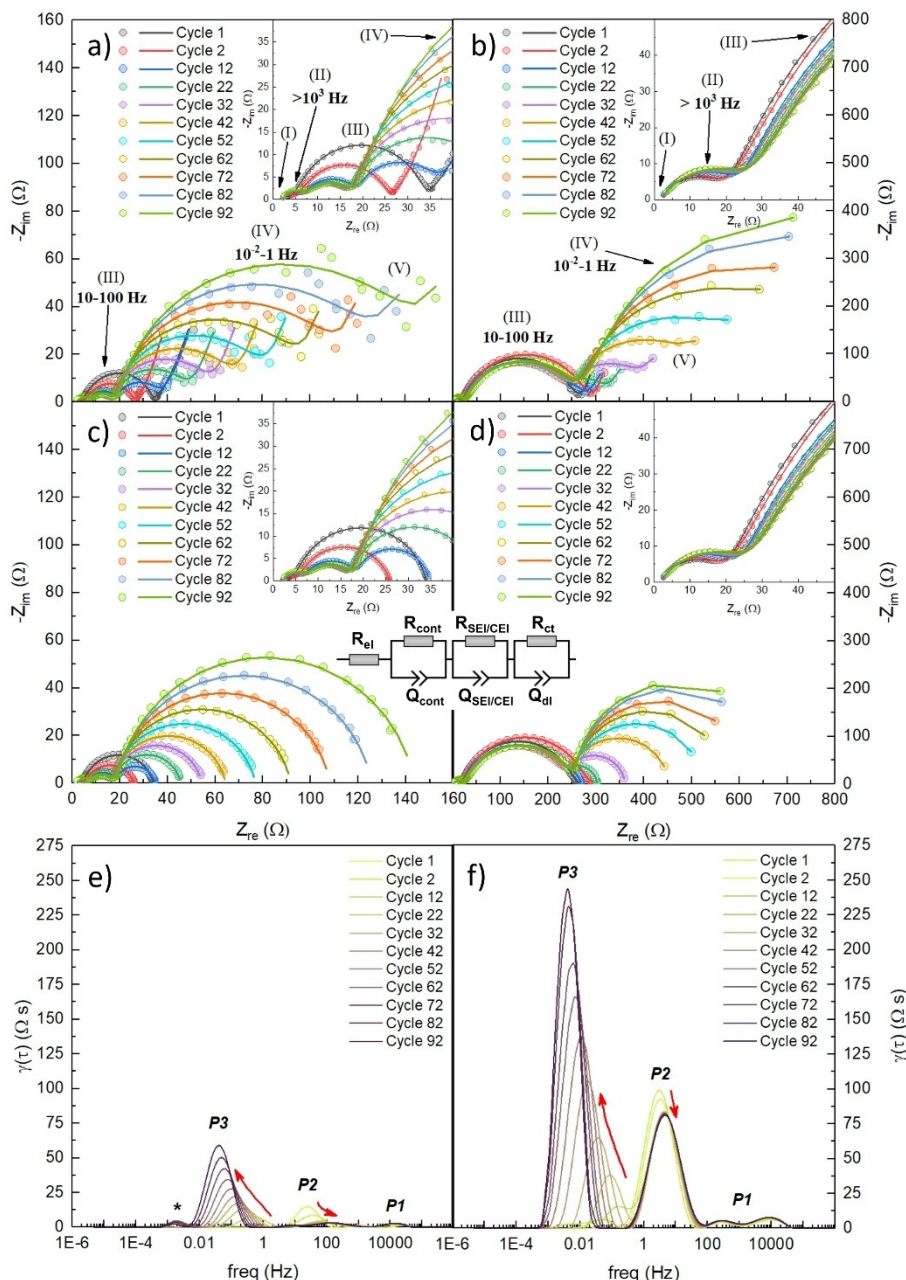


**Figure 10.** Electrochemical impedance spectroscopy analysis of CCDHC | NaMnMO and CCDHC | NaMnMO-SSq full cells, performed at the 1<sup>st</sup>, 2<sup>nd</sup> and every 12<sup>th</sup> cycle in the frequency range  $3 \text{ mHz} < f < 199 \text{ kHz}$ ; Nyquist plots obtained for a) CCDHC | NaMnMO and b) CCDHC | NaMnMO-SSq, with related fits performed according to the R(RC)(RC)(RC)WC model; Nyquist plots after subtraction of the diffusive part displayed for c) CCDHC | NaMnMO and d) CCDHC | NaMnMO-SSq, with related fits and equivalent circuit employed, namely R(RC)(RC)(RC); Distribution of relaxation times for e) CCDHC | NaMnMO and f) CCDHC | NaMnMO-SSq.

centered between 0.1 Hz and 1 Hz for both cells and progressively shifts to lower frequencies. However, the shift is more pronounced for CCDHC | NaMnMO-SSq ( $f < 0.01 \text{ Hz}$ , cycle 92) as compared to CCDHC | NaMnMO ( $0.01 \text{ Hz} < f < 0.1 \text{ Hz}$ , cycle 92). This is consistent with the charge transfer process becoming slower at a faster rate after decomposition of sodium squarate.

Based on the reported data, the fitted values of the circuit elements were plotted as a function of cycle number for

CCDHC | NaMnMO and CCDHC | NaMnMO-SSq (Figure 11), to evidence the behavior of the cells upon cycling.

From the CCDHC | NaMnMO cell in Figure 11a, the resistance of the electrolyte,  $R_{el}$ , displays a constant behavior upon cycling. The resistance of the passivation layers,  $R_{SEI/CEI}$ , shows a lower value in the first cycle due to the SEI/CEI not yet completely formed ( $E_{cell} = 4.00 \text{ V}$ ), and then increases in the second cycle due to the complete formation of SEI and CEI, remaining low and constant after the second cycle. These results suggest the formation of thin passivation layers during

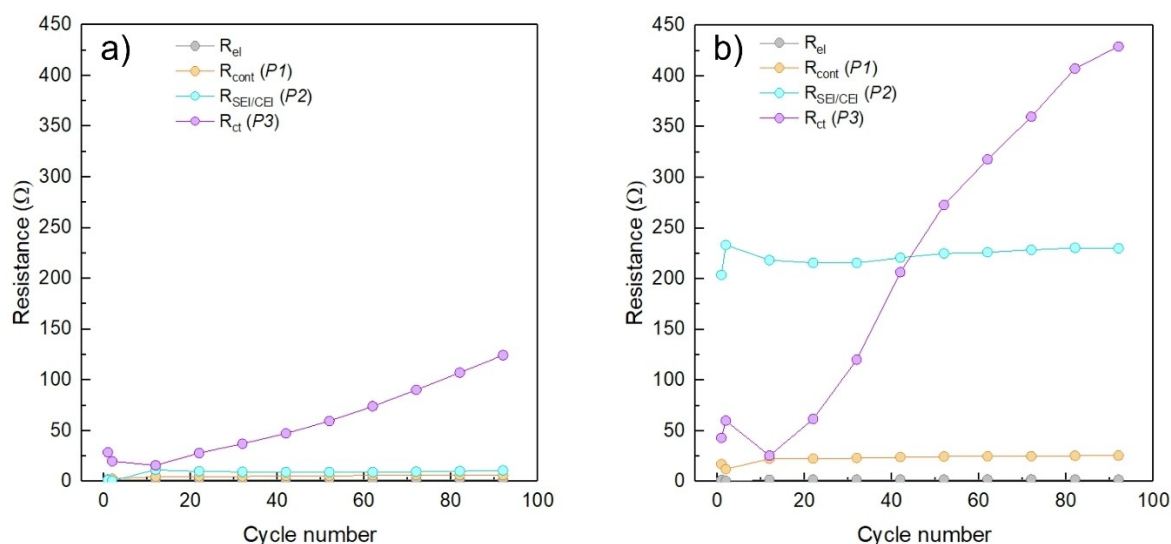


**Figure 11.** Trend of  $R_{el}$ ,  $R_{cont}$ ,  $R_{SEI/CEI}$  and  $R_{ct}$  as a function of cycle number for a) CCDHC || NaMnMO and b) CCDHC || NaMnMO-SSq full cells.

the first charge, which then remain stable in the subsequent cycles, preventing further electrolyte decomposition. As for the resistance to charge transfer,  $R_{ct}$ , an initial decrease is observed when going from the 1<sup>st</sup> to the 10<sup>th</sup> cycle, after which the resistance values start increasing almost at a constant rate. This is probably attributed to the irreversible sodium depletion during SEI formation, which causes an unbalancing in the charges between the electrodes and eventually results in the loss of performance. When considering the presodiated cell in Figure 11b, the resistance of the electrolyte,  $R_{el}$ , is basically the same as the CCDHC || NaMnMO cell, remaining constant upon cycling. The resistance of the passivation layers,  $R_{SEI/CEI}$ , also displays a similar trend, increasing after the first cycle and then remaining constant upon subsequent cycling; however, the order of magnitude of the associated impedance is more than 20 times higher. This result is consistent with what observed from the XPS measurements (Figure 9b–c), indicating the formation of thicker and more insulating SEI/CEI upon squarate decomposition. The effects of such passivation layers are therefore reflected on the charge transfer resistance,  $R_{ct}$ , which starts at similar values as Figure 11a, but increases at a much faster rate as a result of a more sluggish kinetics of the redox processes, hence leading to a faster loss of performance.

## Conclusions

The use of  $\text{Na}_2\text{C}_4\text{O}_4$  as a green and cheap presodiation source in sodium-ion full cells was evaluated for a hard carbon-layered oxide system, namely CCDHC as the anode and  $\text{Na}_{0.66}\text{Mn}_{0.75}\text{Ni}_{0.2}\text{Mg}_{0.05}\text{O}_2$  as the cathode. From the rate capability tests, both electrodes showed high capacity retention and relatively low polarization at low-medium current, with the cathode being able to sustain current densities as high as  $2000 \text{ Mg}^{-1}$ . When tested in full cell configuration, the charge/discharge performance was quite good, though a fast decay

upon cycling was also observed due to the irreversible SEI formation, which was not balanced. When the presodiation additive was employed, a higher initial charge capacity was achieved as a result of an increased amount of sodium provided to compensate the SEI formation and sodium deficiency at the cathode side. However, though in the first cycles the capacity of the CCDHC || NaMnMO-SSq cell exceeds that of the CCDHC || NaMnMO one, a low capacity retention upon long-term cycling was also observed. When comparing the CCDHC || NaMnMO and the CCDHC || NaMnMO-SSq systems, SEM micrographs on pristine and desodiated cathodes revealed the formation of holes and crack formation/growth on the electrode surface after the decomposition of squarate. Moreover, *operando* XRD measurements allowed us to observe differences in the structural evolution of the two cells, revealing that the P2/Z-phase transformation was suppressed or polarized by the higher Na content provided upon presodiation. *Operando* XAS measurements further indicated that the redox activity of Ni was affected by the squarate decomposition, although changes in the oxidation state of Ni from 2+ to 4+ were observed in both systems. Nevertheless, the coordination environment of Ni in CCDHC || NaMnMO-SSq seems to undergo less reversible processes after squarate decomposition. In addition, *ex-situ* XPS analysis on electrodes after the first formation cycle showed a considerable increase of the surface layer thickness both on the positive and negative electrode upon presodiation, as a result of ether and carbonate deposits formation. The hypothesis of a larger surface layer thickness was validated by the EIS measurements, revealing a much higher  $R_{SEI/CEI}$  when squarate was employed and resulting in a faster increase of  $R_{ct}$  and performance decay.

Overall, considering the high loadings employed and the good coulombic efficiencies upon cycling, the combination of NaMnMO and CCDHC could be suitable for full cell applications. The sacrificial salt  $\text{Na}_2\text{C}_4\text{O}_4$  was indeed able to provide additional sodium to compensate the SEI formation at the anode

side and address the sodium deficiency at the cathode side, resulting in a cheaper and greener alternative as compared to using higher mass loadings for the cathode, part of which would remain as a dead weight inside the cell. Although the results obtained in the present work clearly show that some limitations in the presodiation via sacrificial salt must still be overcome, we believe that this aspect could be a suitable object for further studies in order to improve possible practical applications, focusing on the optimization of the presodiation process and of the interfacial and structural stabilities of the materials to eventually achieve longer cycle life with slower capacity fade.

## Experimental

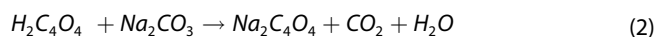
### Synthesis of CCDHC and NaMnMO

The synthetic procedure for the CCDHC anode and P2-layered cathode are the same as reported in previously published papers.<sup>[60,61]</sup> Shortly, CCDHC was synthesized through a carbonization route under inert gas flow at 950 °C for 3 h in a tubular furnace, with a heating ramp of 5 °C min<sup>-1</sup>. The as-obtained carbon was finely ground through a planetary ball-mill for 30 min at 300 rpm in clockwise/counterclockwise mode, to reduce the particle size of the final CCDHC.

As for the cathode powder, the doped P2 Na<sub>0.66</sub>Mn<sub>0.75</sub>Ni<sub>0.2</sub>Mg<sub>0.05</sub>O<sub>2</sub> layered oxide was synthesized through a two-step synthesis. Briefly, Mn<sub>0.75</sub>Ni<sub>0.25</sub>(OH)<sub>2</sub> was first synthesized by co-precipitation in a continuous stirred tank reactor (V = 1 L) by employing a mixture of Ni(NO<sub>3</sub>)<sub>2</sub> · 4H<sub>2</sub>O, Mn(NO<sub>3</sub>)<sub>2</sub> · 6H<sub>2</sub>O, NaOH and NH<sub>3</sub> solution with the appropriate ratios. The obtained precursor was then subjected to a solid-state synthesis step by mixing via wet impregnation with an aqueous solution containing appropriate amounts of NaOH (7 mol L<sup>-1</sup>) and MgCO<sub>3</sub> (3.7 w/w %). The mixture was dried at 140 °C for 3 h and the obtained powder was calcined at 900 °C in a batch furnace for 12 h under air atmosphere followed by cooling to 200 °C. The powder was immediately transferred to a Büchi Glass oven and kept under vacuum at 200 °C overnight. The dried powder was transferred and stored in an Ar-filled glovebox (MBraun) with O<sub>2</sub> and H<sub>2</sub>O content < 0.5 ppm.

### Synthesis of Na<sub>2</sub>C<sub>4</sub>O<sub>4</sub>

The sacrificial additive Na<sub>2</sub>C<sub>4</sub>O<sub>4</sub> (sodium squarate) was synthesized according to the reaction described in Equation (2), by starting from the corresponding acid to produce the sodium salt.



Briefly, stoichiometric amounts of 3,4-dihydroxy-3-cyclobutene-1,2-dione (squaric acid) and Na<sub>2</sub>CO<sub>3</sub> were dissolved in d.i. H<sub>2</sub>O and left stirring overnight at room temperature.<sup>[56]</sup> A Büchi rotavapor was employed to evaporate water, and the obtained white powder was subsequently dried under vacuum at 100 °C for 12 h and finely ground in an agate mortar prior to any use.

### Structural Characterization of NaMnMO and Na<sub>2</sub>C<sub>4</sub>O<sub>4</sub>

The phase purity of the cathode active material, NaMnMO, and of the synthesized Na<sub>2</sub>C<sub>4</sub>O<sub>4</sub> was verified through powder X-ray diffraction (STOE STADI P diffractometer equipped with a Mo–K $\alpha$

radiation source,  $\lambda = 0.709 \text{ \AA}$ , and Debye-Scherrer geometry). All the diffraction patterns were analyzed through Rietveld refinements by using the FullProf software from the WinPLOTR software package.

### Electrode Processing

The slurry for the preparation of NaMnMO electrodes was obtained by mixing the different components in the formulation of 84:8:8 (NaMnMO : PVdF : Super C-65). All the components were first ground together in an agate mortar, added to NMP and left stirring for 4 h to form a homogeneous dispersion, with a 40% solid content. The obtained slurry was coated onto Al foil (15  $\mu\text{m}$  thickness) through doctor blading technique and left drying for 2 h at room temperature and then at 100 °C in a vacuum oven. Finally, circular electrodes of  $\varnothing = 12 \text{ mm}$  and  $\varnothing = 18 \text{ mm}$  were cut by using an electrode puncher with the proper diameter and pressed at 4.42 ton cm<sup>-2</sup> through a hydraulic press. Due to the air and moisture sensitivity of the cathode active material, all the abovementioned procedure was performed inside an Ar-filled glovebox (MBraun) with O<sub>2</sub> and H<sub>2</sub>O content < 0.5 ppm.

The slurries and electrodes for the sole Na<sub>2</sub>C<sub>4</sub>O<sub>4</sub> and NaMnMO-SSq were prepared in the same way as for NaMnMO, with formulations of 65:5:30 (Na<sub>2</sub>C<sub>4</sub>O<sub>4</sub> : PVdF : Super C-65) and 64.6:23.28:6.06:6.06 (NaMnMO : Na<sub>2</sub>C<sub>4</sub>O<sub>4</sub> : PVdF : Super C-65), respectively. Electrodes for *operando* XRD measurements of NaMnMO and NaMnMO-SSq were prepared by coating onto carbon paper current collector rather than Al foil, in order to avoid any signals from the current collector.

The slurry for the preparation of CCDHC electrodes was obtained by mixing the components in the formulation 93:5.6:1.4 (CCDHC : CMC/SBR (1:2) : Super C-65). The powders of CCDHC and Super C-65 were first dry-mixed through a SpeedMixer (DAC 150 FVZ–K) for 15 min at 300 rpm. A 2% CMC solution in d.i. H<sub>2</sub>O was then added to the powders and stirred at 1500 rpm for 45 min. Finally, a 39% SBR emulsion was also added, together with a proper amount of d.i. H<sub>2</sub>O to obtain a final solid content of 43%, and the dispersion was stirred at 500 rpm for 15 min. The obtained slurry was coated onto Al foil (15  $\mu\text{m}$  thickness) through doctor blading technique and left drying overnight at room temperature. The coating was then calendared by applying a force of 50 kN at 50 °C in order to have a 10% thickness reduction. Finally, circular electrodes of  $\varnothing = 12 \text{ mm}$  and  $\varnothing = 18 \text{ mm}$  were cut by using an electrode puncher with the proper diameter and vacuum-dried at 110 °C overnight.

For full cell measurements, the wet thicknesses of the cathodic and anodic coatings were adjusted to provide charge balancing between positive and negative electrode (without considering SEI contribution), maintaining a slight excess of the latter to prevent plating effects. The mass loadings of the electrodes employed in the full cells ranged from 9 to 11 mg cm<sup>-2</sup> for NaMnMO and 6 to 7 mg cm<sup>-2</sup> for CCDHC.

### Electrochemical Measurements

Most of the electrochemical measurements for NaMnMO, Na<sub>2</sub>C<sub>4</sub>O<sub>4</sub>, NaMnMO-SSq, CCDHC half-cells, and the related CCDHC || NaMnMO and CCDHC || NaMnMO-SSq full cells, were carried out by using three-electrode Swagelok-type cells, with sodium metal serving as reference (both half and full cells) and counter electrode (only half-cells). Modified two-electrode CR2032 coin-type cells were employed for *operando* XRD and synchrotron XAS measurements of NaMnMO and NaMnMO-SSq. Three-electrode PAT-Cells (EL-Cell) with preassembled sodium metal disk reference electrode were employed for impedance measurements on CCDHC || NaMnMO

and CCDHC||NaMnMO-SSq full cells. Whatman GF/D fiberglass separators were used for all the measurements, besides *ex-situ* XPS and intermittent SEM, where a cellulose separator was chosen in order to avoid the presence of fiberglass residues on the electrode surface after cycling. All cells were assembled in a high-purity Argon-filled glovebox (MBraun) with O<sub>2</sub> and H<sub>2</sub>O content < 0.5 ppm. The electrolyte employed was 1 M NaPF<sub>6</sub> dissolved in a 1:1 mol/mol mixture of ethylene carbonate and propylene carbonate (EC:PC) for all cells tested, with the addition of 5% w/w fluoroethylene carbonate (FEC) only for half-cell measurements in order to stabilize the sodium metal from the counter electrode.<sup>[66]</sup> All electrochemical measurements were performed using a VMP-3 multichannel electrochemical workstation with an integrated frequency response analyzed by Bio-Logic. Cyclic voltammeteries were acquired at a scan rate of 0.1 mV s<sup>-1</sup> for all cells. The charge-discharge performance of all materials in both half-cell and full cell configurations were evaluated by galvanostatic cycling the electrodes for 2 formation cycles at 10 mA g<sup>-1</sup> and then 20 mA g<sup>-1</sup> for 100 cycles; for full cells, a slight anode excess was kept, and the applied current density was normalized according to the cathode active material mass. Rate capability tests were performed by galvanostatically cycling the materials with specific currents ranging from 10 mA g<sup>-1</sup> to 2000 mA g<sup>-1</sup>. The cycling tests for NaMnMO, Na<sub>2</sub>C<sub>4</sub>O<sub>4</sub> and NaMnMO-SSq half-cells were performed within the voltage window 2.70 V < E < 4.30 V, while those for CCDHC were performed within the window 0.01 V < E < 1.50 V. For the electrochemical tests performed on NaMnMO-SSq, the cells were brought inside the glovebox after one full cycle and opened to remove the CO<sub>2</sub> formed during presodiation, thus avoiding any unwanted polarizations in the following cycles due to the increased pressure from gas evolution. For the full cells, a three-electrode setup was employed to control the cell potential while monitoring the anode and cathode ones, with a voltage window chosen by calculating the difference between the cut-offs of the single electrodes (i.e. 1.20 V < E < 4.29 V). Electrochemical impedance spectroscopy (EIS) measurements were acquired upon cycling in potentiostatic mode during the 1<sup>st</sup>, 2<sup>nd</sup> and every 12<sup>th</sup> cycle at bias potentials E<sub>cell</sub> = 4.00 V. For all EIS measurements, a sinusoidal perturbation of ΔE = ±10 mV was applied over the frequency range 3 mHz < f < 199 kHz, with 10 points per decade and logarithmic spacing. The low-frequency diffusion region was subtracted from the obtained Nyquist plots in order to calculate the function of distribution of relaxation times (DRT). The fitting procedure by Equivalent Circuit Method (ECM) and the calculation of the DRT function (Tikhonov regularization, λ = 10<sup>-2</sup>) were performed by using the software RelaxIS3. All the potential values in the half-cells are referred to the Na<sup>+</sup>/Na redox couple (E° = -2.71 V vs. RHE).

### Morphological Characterization

The evolution of the electrode morphology on electrodes of NaMnMO and NaMnMO-SSq (both pristine and after the first desodiation in full cell configuration) were performed by scanning electron microscopy (Zeiss Merlin) in order to observe the electrode surface after sodium squarate decomposition and gas evolution. The full cells were charged by applying a specific current of 10 mA g<sup>-1</sup><sub>cat</sub>, transferred into an Ar-filled glovebox (MBraun) with O<sub>2</sub> and H<sub>2</sub>O content < 0.5 ppm, and the electrodes were washed in dimethyl carbonate (DMC) prior to investigation. A vacuum-transfer system (Leica EM VCT100) was used to transfer the electrodes from the glovebox to the microscope avoiding exposure to air.

### Ex-situ and Operando Measurements

*Ex-situ* X-ray photoelectron spectroscopy (XPS) measurements on electrodes of NaMnMO, NaMnMO-SSq and CCDHC (both pristine and after one cycle in full cell configuration) were conducted through a K-alpha spectrometer from Thermo-Fisher Scientific equipped with a micro-focused, monochromated Al-Kα X-ray source with 400 μm spot size. A pass energy of 50 eV was used. Data acquisition and elaboration was performed via the Thermo Advantage software,<sup>[96]</sup> and the obtained spectra were fitted through one or more Voigt profiles. Quantification was performed by applying Scofield sensitivity factors, and all spectra were referenced in binding energy to the hydrocarbon C 1s peak at 285 eV. For the sake of clarity, all spectra were normalized to the maximum intensity (i.e., highest peak and background are normalized to [1,0]). In order to analyze the effect of Na<sub>2</sub>C<sub>4</sub>O<sub>4</sub> on the SEI and CEI composition, the full cells were charged and discharged by applying a specific current of 10 mA g<sup>-1</sup><sub>cat</sub> and a 1 h constant voltage step was employed at the discharge endpoint potential to ensure SEI/CEI stability. The cells were transferred into an Ar-filled glovebox (MBraun) with O<sub>2</sub> and H<sub>2</sub>O content < 1.0 ppm, and the electrodes were recovered and washed by a 1-minute submersion in dimethyl carbonate (DMC). After washing, all electrodes were dried and mounted on a sample holder using a conductive Cu tape. The transfer to the XP spectrometer was performed through a transfer module under inert gas conditions.

In order to evaluate the effect of Na<sub>2</sub>C<sub>4</sub>O<sub>4</sub> on the stability of phase transitions, *operando* X-ray diffraction was carried out on NaMnMO and NaMnMO-SSq half-cells during the first two cycles at 10 mA g<sup>-1</sup>, through a high-energy and high-angular-resolution STOE diffractometer equipped with Ag-Kα radiation source, λ = 0.559 Å, two Mythen detectors and a dedicated coin cell setup,<sup>[97]</sup> in transmission geometry. The modified coin cells acted as sample containers rotating continuously to improve the crystallite statistics. Diffraction patterns were collected in the scattering range 0° < 2θ < 36° with 0.005° intervals and a dwell time of 20 min.

*Operando* XAS measurements were performed at synchrotron beamlines P64 at PETRA III (DESY), Hamburg. The Mn and Ni K-edge for NaMnMO and NaMnMO-SSq were measured, and the energy was calibrated by using a corresponding Mn or Ni foil, as commonly applied in XAS experiments. MnO, Mn<sub>2</sub>O<sub>3</sub>, MnO<sub>2</sub> and NiO were used as standard materials. All data were collected at room temperature with a Si(111) double crystal monochromator, and all XAS spectra were processed by using the DEMETER software package.<sup>[98]</sup> A modified CR2032 coin cell setup with Kapton windows (Ø = 6 mm) was used to cycle the cells at 10 mA g<sup>-1</sup> to investigate the first two cycles.

### Acknowledgements

This work contributes to the research performed at CELEST (Center for Electrochemical Energy Storage Ulm-Karlsruhe) and was funded by the German Research Foundation (DFG) under Project ID 390874152 (POLiS Cluster of Excellence). We acknowledge the synchrotron radiation source PETRA-III (DESY) in Hamburg, Germany, for the provision of beamtime at the P64 beamline. We greatly appreciate Mrs. Liuda Mereacre for the *operando* coin cell production and Dr. Oleksandr Dolotko for the *operando* XRD measurements.

## Conflict of Interests

The authors declare no conflict of interest.

## Data Availability Statement

The data that support the findings of this study are openly available in KIT Library at <https://doi.org/10.5281/zenodo.10161577>.

**Keywords:** Sodium-ion · Presodiation · Squarate · Layered Oxide · Hard Carbon

- [1] J. T. Lee, D. S. Callaway, *Nat. Energy* **2018**, 3(11), 960–968.
- [2] B. Dunn, H. Kamath, J. M. Tarascon, *Science* **2011**, 334(6058), 928–935.
- [3] S. Chu, A. Majumdar, *Nature* **2012**, 488(7411), 294–303.
- [4] R. L. Fares, M. E. Webber, *Nat. Energy* **2017**, 2, 17001.
- [5] V. Palomares, P. Serras, I. Villaluenga, K. B. Hueso, J. Carretero-González, T. Rojo, *Energy Environ. Sci.* **2012**, 5(3), 5884–5901.
- [6] H. Pan, Y. S. Hu, L. Chen, *Energy Environ. Sci.* **2013**, 6(8), 2338–2360.
- [7] C. Nithya, S. Gopukumar, *Wiley Interdiscip. Rev. Energy Environ.* **2015**, 4(3), 253–278.
- [8] H. Chen, T. N. Cong, W. Yang, C. Tan, Y. Li, Y. Ding, *Prog. Nat. Sci.* **2009**, 19(3), 291–312.
- [9] V. Etacheri, R. Marom, R. Elazari, G. Salitra, D. Aurbach, *Energy Environ. Sci.* **2011**, 4(9), 3243–3262.
- [10] M. S. Dresselhaus, I. L. Thomas, *Nature* **2001**, 414, 332–337.
- [11] M. Perrin, Y. M. Saint-Drenan, F. Mattera, P. Malbranche, *J. Power Sources* **2005**, 144(2), 402–410.
- [12] D. Kundu, E. Talaie, V. Duffort, L. F. Nazar, *Angew. Chemie - Int. Ed.* **2015**, 54(11), 3432–3448.
- [13] J. Y. Hwang, S. T. Myung, Y. K. Sun, *Chem. Soc. Rev.* **2017**, 46(12), 3529–3614.
- [14] A. Eftekhari, D. W. Kim, *J. Power Sources* **2018**, 395, 336–348.
- [15] C. Liu, F. Li, M. Lai-Peng, H. M. Cheng, *Adv. Mater.* **2010**, 22(8), 28–62.
- [16] R. Usiskin, Y. Lu, J. Popovic, M. Law, P. Balaya, Y. S. Hu, J. Maier, *Nat. Rev. Mater.* **2021**, 6(11), 1020–1035.
- [17] W. Zuo, Y. Yang, *Accounts Mater. Res.* **2022**, 3(7), 709–720.
- [18] A. Ramesh, A. Tripathi, P. Balaya, *J. Appl. Ceram. Technol.* **2022**, 19(2), 913–923.
- [19] P. F. Wang, H. R. Yao, X. Y. Liu, Y. X. Yin, J. N. Zhang, Y. Wen, X. Yu, L. Gu, Y. G. Guo, *Sci. Advances* **2018**, 4(3), 1–9.
- [20] T. Jin, H. Li, K. Zhu, P. F. Wang, P. Liu, L. Jiao, *Chem. Soc. Rev.* **2020**, 49(8), 2342–2377.
- [21] J. Peng, W. Zhang, Q. Liu, J. Wang, S. Chou, H. Liu, S. Dou, *Adv. Mater.* **2022**, 34(15), 1–20.
- [22] T. Akçay, M. Häringer, K. Pfeiffer, J. Anhalt, J. R. Binder, S. Dsoke, D. Kramer, R. Mönig, *ACS Appl. Energy Mater.* **2021**, 4(11), 12688–12695.
- [23] W. Zuo, A. Innocenti, M. Zarrabeitia, D. Bresser, Y. Yang, S. Passerini, *Acc. Chem. Res.* **2023**, 56(3), 284–296.
- [24] C. Delmas, C. Fouassier, P. Hagenmuller, *Phys. B + C* **1980**, 99(1–4), 81–85.
- [25] H. Wang, B. Yang, X. Z. Liao, J. Xu, D. Yang, Y. S. He, Z. F. Ma, *Electrochim. Acta* **2013**, 113, 200–204.
- [26] N. Yabuuchi, M. Yano, H. Yoshida, S. Kuze, S. Komaba, *J. Electrochem. Soc.* **2013**, 160(5), A3131–A3137.
- [27] J. Xu, S. L. Chou, J. L. Wang, H. K. Liu, S. X. Dou, *ChemElectroChem* **2014**, 1(2), 371–374.
- [28] L. Minnetti, V. Marangon, P. Andreotti, A. Staffolani, F. Nobili, J. Hassoun, *Electrochim. Acta* **2023**, 452, 142263.
- [29] X. Liu, W. Zuo, B. Zheng, Y. Xiang, K. Zhou, Z. Xiao, P. Shan, J. Shi, Q. Li, G. Zhong, R. Fu, Y. Yang, *Angew. Chemie. Int. Ed.* **2019**, 58(50), 18086–18095.
- [30] N. Yabuuchi, H. Yoshida, S. Komaba, *Electrochemistry* **2012**, 80(10), 716–719.
- [31] E. Lee, D. E. Brown, E. E. Alp, Y. Ren, J. Lu, J. J. Woo, C. S. Johnson, *Chem. Mater.* **2015**, 27(19), 6755–6764.
- [32] J. Xu, S. L. Chou, J. L. Wang, H. K. Liu, S. X. Dou, *ChemElectroChem* **2014**, 1(2), 371–374.
- [33] W. Zuo, X. Liu, J. Qiu, D. Zhang, Z. Xiao, J. Xie, F. Ren, J. Wang, Y. Li, G. F. Ortiz, W. Wen, S. Wu, M. S. Wang, R. Fu, Y. Yang, *Nat. Commun.* **2021**, 12(1), 1–11.
- [34] R. Zhang, S. Yang, H. Li, T. Zhai, H. Li, *InfoMat* **2022**, 4(6), 1–26.
- [35] X. Wu, J. Guo, D. Wang, G. Zhong, M. J. McDonald, Y. Yang, *J. Power Sources* **2015**, 281, 18–26.
- [36] Y. J. Guo, P. F. Wang, Y. Bin Niu, X. D. Zhang, Q. Li, X. Yu, M. Fan, W. P. Chen, Y. Yu, X. Liu, Q. Meng, S. Xin, Y. X. Yin, Y. G. Guo, *Nat. Commun.* **2021**, 12(1), 1–11.
- [37] D. Di Lecce, D. Campanella, J. Hassoun, *J. Phys. Chem. C* **2018**, 122(42), 23925–23933.
- [38] H. Darjazi, A. Staffolani, L. Sbrascini, L. Bottoni, R. Tossici, F. Nobili, *Energies* **2020**, 13(23), 6216.
- [39] H. Darjazi, L. Bottoni, H. R. Moazami, S. J. Rezvani, L. Balducci, L. Sbrascini, A. Staffolani, A. Tombesi, F. Nobili, *Mater. Today Sustain.* **2023**, 21, 100313.
- [40] L. Sbrascini, A. Staffolani, L. Bottoni, H. Darjazi, L. Minnetti, M. Minicucci, F. Nobili, *ACS Appl. Mater. Interfaces* **2022**, 14, 33257–33273.
- [41] M. Winter, J. O. Besenhard, in *Handbook of Battery Materials*, Vol.1 (Eds.: C. Daniel, J. O. Besenhard), Wiley-VCH, Weinheim, **2011**, 433–478.
- [42] T. Nakayama, S. Komaba, T. Ozeki, W. Murata, A. Ogata, K. Gotoh, T. Ishikawa, N. Yabuuchi, K. Fujiwara, *Adv. Funct. Mater.* **2011**, 21(20), 3859–3867.
- [43] J. Zhao, L. Zhao, K. Chihara, S. Okada, J. I. Yamaki, S. Matsumoto, S. Kuze, K. Nakane, *J. Power Sources* **2013**, 244, 752–757.
- [44] Z. Song, K. Zou, X. Xiao, X. Deng, S. Li, H. Hou, X. Lou, G. Zou, X. Ji, *Chem. - A Eur. J.* **2021**, 27(65), 16082–16092.
- [45] J. Martínez De Ilarduya, L. Otaegui, M. Galcerán, L. Acebo, D. Shanmukaraj, T. Rojo, M. Armand, *Electrochim. Acta* **2019**, 321, 1–9.
- [46] J. M. De Ilarduya, L. Otaegui, J. M. L. Del Amo, M. Armand, G. Singh, *J. Power Sources* **2017**, 337, 197–203.
- [47] K. Park, B. C. Yu, J. B. Goodenough, *Chem. Mater.* **2015**, 27(19), 6682–6688.
- [48] Y. J. Guo, Y. Bin Niu, Z. Wei, S. Y. Zhang, Q. Meng, H. Li, Y. X. Yin, Y. G. Guo, *ACS Appl. Mater. Interfaces* **2021**, 13(2), 2772–2778.
- [49] X. Liu, Y. Tan, W. Wang, P. Wei, Z. W. Seh, Y. Sun, *ACS Appl. Mater. Interfaces* **2021**, 13(23), 27057–27065.
- [50] P. Jezowski, O. Crosnier, T. Brousse, *Open Chem.* **2021**, 19(1), 432–441.
- [51] P. Jezowski, A. Chojnacka, X. Pan, F. Béguin, *Electrochim. Acta* **2021**, 375, 137980.
- [52] D. Shanmukaraj, K. Kretschmer, T. Sahu, W. Bao, T. Rojo, G. Wang, M. Armand, *ChemSusChem* **2018**, 11(18), 3286–3291.
- [53] X. Liu, Y. Tan, T. Liu, W. Wang, C. Li, J. Lu, Y. Sun, *Adv. Funct. Mater.* **2019**, 29, 1903795.
- [54] K. Zou, W. Deng, P. Cai, X. Deng, B. Wang, C. Liu, J. Li, H. Hou, G. Zou, X. Ji, *Adv. Funct. Mater.* **2021**, 31, 2005581.
- [55] X. Pan, A. Chojnacka, F. Béguin, *Energy Storage Mater.* **2021**, 40, 22–30.
- [56] M. Arnaiz, D. Shanmukaraj, D. Carriazo, D. Bhattacharjya, A. Villaverde, M. Armand, J. Ajouria, *Energy Environ. Sci.* **2020**, 13(8), 2441–2449.
- [57] W. M. Dose, C. S. Johnson, *Curr. Opin. Electrochem.* **2022**, 31, 100827.
- [58] S. Zhang, R. Cao, X. Pu, A. Zhao, W. Chen, C. Song, Y. Fang, Y. Cao, *J. Energy Chem.* **2024**, 92, 162–175.
- [59] J. M. De Ilarduya, L. Otaegui, M. Galcerán, L. Acebo, D. Shanmukaraj, T. Rojo, M. Armand, *Electrochim. Acta* **2019**, 321, 134693.
- [60] C. Gauckler, M. Dillenz, F. Maroni, L. F. Pfeiffer, J. Biskupek, M. Sotoudeh, Q. Fu, U. Kaiser, S. Dsoke, H. Euchner, P. Axmann, M. Wohlfahrt-Mehrens, A. Groß, M. Marinaro, *ACS Appl. Energy Mater.* **2022**, 5(11), 13735–13750.
- [61] L. Bottoni, H. Darjazi, L. Sbrascini, A. Staffolani, S. Gabrielli, G. Pastore, A. Tombesi, F. Nobili, *ChemElectroChem* **2023**, 10(8), e202201117.
- [62] Y.-F. Liu, K. Han, D.-N. Peng, L.-Y. Kong, Y. Su, H.-W. Li, H.-Y. Hu, J.-Y. Li, H.-R. Wang, Z.-Q. Fu, Q. Ma, Y.-F. Zhu, R.-R. Tang, S.-L. Chou, Y. Xiao, X.-W. Wu, *InfoMat* **2023**, 5(6), e12422.
- [63] L. F. Pfeiffer, N. Jobst, C. Gauckler, M. Lindén, M. Marinaro, S. Passerini, M. Wohlfahrt-Mehrens, P. Axmann, *Front. Energy Res.* **2022**, 10, 1–17.
- [64] R. E. Dinnebier, H. Nuss, M. Jansen, *Zeitschrift für Krist.* **2005**, 220(11), 954–961.
- [65] M. Han, C. Zhu, T. Ma, Z. Pan, Z. Tao, J. Chen, *Chem. Commun.* **2018**, 54(19), 2381–2384.
- [66] K. Pfeiffer, S. Arnold, J. Becherer, C. Das, J. Maibach, H. Ehrenberg, S. Dsoke, *ChemSusChem* **2019**, 12(14), 3312–3319.
- [67] L. Zhang, C. Wang, Y. Liu, M. Ren, J. Du, A. Chen, F. Li, *Chem. Eng. J.* **2021**, 426, 130813.
- [68] I. Hasa, D. Buchholz, S. Passerini, J. Hassoun, *ACS Appl. Mater. Interfaces* **2015**, 7(9), 5206–5212.

- [69] R. Luo, F. Wu, M. Xie, Y. Ying, J. Zhou, Y. Huang, Y. Ye, L. Li, R. J. Chen, *J. Power Sources* **2018**, *383*, 80–86.
- [70] K. Wang, P. Yan, M. Sui, *Nano Energy* **2018**, *54*, 148–155.
- [71] A. Gutierrez, W. M. Dose, O. Borkiewicz, F. Guo, M. Avdeev, S. Kim, T. T. Fister, Y. Ren, J. Kumakura, Y. Yoda, K. Kuroki, S. Komaba, *Adv. Energy Mater.* **2018**, *8*(17), 1–30.
- [72] F. Xie, Z. Xu, Z. Guo, M. M. Titirici, *Prog. Energy* **2020**, *2*(4), 042002.
- [73] D. Chen, D. Kramer, R. Mönig, *Electrochim. Acta* **2018**, *259*, 939–948.
- [74] K. Kubota, S. Kumakura, Y. Yoda, K. Kuroki, S. Komaba, *Adv. Energy Mater.* **2018**, *8*(17), 1–30.
- [75] G. Singh, N. Tapia-Ruiz, J. M. L. Del Amo, U. Maitra, J. W. Somerville, A. R. Armstrong, J. M. De Ilarduya, T. Rojo, P. G. Bruce, *Chem. Mater.* **2016**, *28*(14), 5087–5094.
- [76] N. Tapia-Ruiz, W. M. Dose, N. Sharma, H. Chen, J. Heath, J. W. Somerville, U. Maitra, M. S. Islam, P. G. Bruce, *Energy Environ. Sci.* **2018**, *11*(6), 1470–1479.
- [77] J. W. Somerville, A. Sobkowiak, N. Tapia-Ruiz, J. Billaud, J. G. Lozano, R. A. House, L. C. Gallington, T. Ericsson, L. Haggstrom, M. R. Roberts, U. Maitra, P. G. Bruce, *Energy Environ. Sci.* **2019**, *12*, 2223–2232.
- [78] W. Zuo, J. Qiu, C. Hong, X. Liu, J. Li, G. F. Ortiz, Q. Li, S. Zheng, G. R. Zheng, Y. Yang, *ACS Appl. Energy Mater.* **2019**, *2*(7), 4914–4924.
- [79] C. Zhao, Z. Yao, Q. Wang, H. Li, J. Wang, M. Liu, S. Ganapathy, Y. Lu, J. Cabana, B. Li, X. Bai, A. Aspuru-Guzik, M. Wagemaker, L. Chen, Y. S. Hu, *J. Am. Chem. Soc.* **2020**, *142*(12), 5742–5750.
- [80] B. Zhou, D. Wong, Z. Fu, H. Guo, C. Schulz, G. Karkera, H. Hahn, M. Bianchini, Q. Wang, *Small* **2024**, 2402991.
- [81] S. Yuan, L. Yu, G. Qian, Y. Xie, P. Guo, G. Cui, J. Ma, X. Ren, Z. Xu, S.-J. Lee, J.-S. Lee, Y. Liu, Y. Ren, L. Li, G. Tan, X. Liao, *Nano Lett.* **2023**, *23*, 1743–1751.
- [82] N. K. Karan, M. D. Slater, F. Dogan, D. Kim, C. S. Johnson, M. Balasubramanian, *J. Electrochem. Soc.* **2014**, *161*, A1107.
- [83] R. J. Clément, J. Xu, D. S. Middlemiss, J. Alvarado, C. Ma, Y. S. Meng, C. P. Grey, *J. Mater. Chem. A* **2017**, *5*(8), 4129–4143.
- [84] N. Yabuuchi, K. Yoshii, S. T. Myung, I. Nakai, S. Komaba, *J. Am. Chem. Soc.* **2011**, *133*(12), 4404–4419.
- [85] Z. Cheng, B. Zhao, Y. J. Guo, L. Yu, B. Yuan, W. Hua, Y. X. Yin, S. Xu, B. Xiao, X. Han, P. F. Wang, Y. G. Guo, *Adv. Energy Mater.* **2022**, *12*(14), 1–9.
- [86] S. Hy, H. Liu, M. Zhang, D. Qian, B. J. Hwang, Y. S. Meng, *Energy Environ. Sci.* **2016**, *9*(6), 1931–1954.
- [87] H. Yu, H. Zhou, *J. Phys. Chem. Lett.* **2013**, *4*(8), 1268–1280.
- [88] J. Maibach, F. Jeschull, D. Brandell, K. Edström, M. Valvo, *ACS Appl. Mater. Interfaces* **2017**, *9*, 12373–12381.
- [89] P. Swift, *Surf. Interface Anal.* **1982**, *4*(2), 47–51.
- [90] I. D. Raistrick, D. R. Franceschetti, J. R. Macdonald, in *Impedance Spectroscopy - Theory, Experiment, and Applications*, Vol.1 (Eds.: E. Barsoukov, J. R. Macdonald), Wiley-Interscience, **2005**, 80–117.
- [91] B. A. Boukamp, *Solid State Ionics* **1986**, *20*, 31–34.
- [92] B. A. Boukamp, *Solid State Ionics* **1986**, *18–19*, 136–140.
- [93] A. L. Gavriluk, D. A. Osinkin, D. I. Bronin, *Russ. J. Electrochem.* **2017**, *53*(6), 575–588.
- [94] A. Staffolani, A. Baldinelli, G. Bidini, F. Nobili, L. Barelli, *Energies* **2022**, *15*(14), 4978.
- [95] L. Minnetti, L. Sbrascini, A. Staffolani, V. Marangon, F. Nobili, J. Hassoun, *J. Energy Chem.* **2024**, *96*, 300–317.
- [96] K. L. Parry, A. G. Shard, R. D. Short, R. G. White, J. D. Whittle, A. Wright, *Surf. Interface Anal.* **2006**, *38*(11), 1497–1504.
- [97] M. Herklotz, J. Weiß, E. Ahrens, M. Yavuz, L. Mereacre, N. Kiziltas-Yavuz, C. Dräger, H. Ehrenberg, J. Eckert, F. Fauth, L. Giebeler, M. Knapp, *J. Appl. Crystallogr.* **2016**, *49*, 340–345.
- [98] B. Ravel, M. Newville, *J. Synchrotron Radiat.* **2005**, *12*(4), 537–541.

Manuscript received: May 15, 2024

Revised manuscript received: July 12, 2024

Accepted manuscript online: July 15, 2024

Version of record online: November 6, 2024